Astron. Astrophys. 361, 641–659 (2000)

ASTRONOMY AND ASTROPHYSICS

A systematic investigation of the mass loss mechanism in dust forming long–period variable stars⋆

J.M. Winters[1,2,3], **T. Le Bertre**[1], **K.S. Jeong**[3], **Ch. Helling**[3], **and E. Sedlmayr**[3]

[1] DEMIRM, UMR 8540, Observatoire de Paris, 61 av. de l'Observatoire, 75014 Paris, France
[2] Max-Planck-Institut für Radioastronomie, Auf dem Hügel 69, 53121 Bonn, Germany
[3] Technische Universität Berlin, Institut für Astronomie und Astrophysik, PN 8-1, Hardenbergstrasse 36, 10623 Berlin, Germany

Received 28 April 2000 / Accepted 19 July 2000

Abstract. In order to investigate the relations between the mass loss from pulsating red giants and quantities which can be obtained from observations, we have explored the behavior of theoretical models which treat the time-dependent hydrodynamics of circumstellar outflows, including a detailed treatment of the dust formation process. This approach, while ignoring effects such as a possible non-sphericity of the stellar atmospheres which are difficult to assess, accounts correctly for factors such as the grain formation and destruction which are crucial to the mass-loss mechanism.

We built a grid of $\sim$ 150 models covering a wide range of physical situations. This grid allows us to characterize the effects of different parameters, such as the stellar luminosity and temperature, the period and the amplitude of the pulsation, and the C/O element abundance ratio, on the behavior of AGB winds and on the rates of mass loss.

We find two regimes for the stellar outflows. The first one (A) is characterized by stable winds with a layered structure of the circumstellar dust shell, outflow velocities in excess of $5\,\mathrm{km\,s^{-1}}$, and a large rate of mass loss. These outflows are dominated by radiation pressure on dust. For these models we find good correlations between near-infrared colors and the mass loss rates. In the second regime (B), the winds are slow and do not present a layered structure. The outflows displaying the second behavior come, e.g., from red giants with low luminosity, high temperature, or short period. For them there is no correlation between color and mass loss rate. The mass loss rates are low and never exceed $3\,10^{-7} M_{\odot}\mathrm{yr}^{-1}$. Radiation pressure on dust plays only a minor role in this regime.

We have explored the effect of different parameters on the behavior of the stellar winds. We find that, in general, all other parameters been kept identical, there is a narrow range of values for each parameter within which the models abruptly change from B to A, and that once a model is stabilized in the A mode the changes in the values of each parameter have only a smooth effect on the wind characteristics.

Send offprint requests to: J.M. Winters (winters@mesioc.obspm.fr)

⋆ Table 2 is only available in electronic form at the CDS via anonymous ftp to cdsarc.u-strasbg.fr (130.79.128.5) or via http://cdsweb.u-strasbg.fr/Abstract.html

Key words: hydrodynamics – stars: winds, outflows – stars: carbon – stars: circumstellar matter – stars: mass-loss – stars: AGB and post-AGB

1. Introduction

Red giants are often surrounded by circumstellar shells. The material in these shells, mainly gas but also dust, is flowing outwards with velocities in the range 5–40 $\mathrm{km\,s^{-1}}$. Thus they are undergoing mass loss at rates which can be as large as a few $10^{-4}\,\mathrm{M_{\odot}\,yr^{-1}}$ (e.g., Lépine et al. 1995). It is not known if there is a lower limit to this phenomenon. From the presence of gaps in the distributions of sources observed in infrared color-color diagrams (e.g. Epchtein et al. 1987, van der Veen & Habing 1988), it has been argued that the mass loss phenomenon could only be stable above some minimum rate of a few $10^{-8}\,\mathrm{M_{\odot}\,yr^{-1}}$. The existence of a lower limit for *radiation driven* winds would be in agreement with theoretical considerations, which predict a minimum mass loss rate of the order of $10^{-7}\,\mathrm{M_{\odot}\,yr^{-1}}$ for *purely dust-driven* winds (Gail & Sedlmayr 1987, Dominik et al. 1990, see also Lamers & Cassinelli 1999, Chap. 7). On the other hand, Omont et al. (1999) discovered a new population of dust forming sources in the Bulge of our Galaxy with very low mass loss rates around $10^{-9}\,\mathrm{M_{\odot}\,yr^{-1}}$. Furthermore, Chan et al. (1998) suggested the existence, also in the Bulge, of a large number of evolved stars ($\sim 850\,\mathrm{L_{\odot}}$) with large mass loss rates.

Among red giants, stars on the Asymptotic Giant Branch (AGB) are particularly important. It is during this phase that low (initial) mass stars ($M_{\mathrm{i}} \leq 6$–$8 M_{\odot}$) lose most of their matter before terminating their evolution as white dwarf remnants (e.g., Olofsson 1999). Also, stars in this evolutionary phase appear to be the main contributors to the replenishment of the interstellar medium (ISM), possibly $\sim$70% in the Solar Neighborhood (Sedlmayr 1994). As the material returned to the ISM has been enriched in elements processed in the stellar interiors, AGB stars play a major rôle in the chemical enrichment of the Galaxy. For instance, most of the carbon found in the Universe should have been synthesized in the interiors of passed AGB stars.

To understand the evolution of stellar populations, it is essential to evaluate the contribution of the different kinds of red giants to the cosmic cycle of matter. Several methods have been proposed and used to determine the mass loss rates from red giants. They all rely on a modeling of the circumstellar shell emission (emission by dust in the infrared or emission by molecules in the radio range) and on an estimate of the object's distance. Therefore, these methods can be applied only to well studied sources. Recently, Le Bertre & Winters (1998) found relations between the mass loss rate and some near-infrared colors. As the colors are distance independent, these relations can be applied in principle to large samples of stars for which little information is available.

In this paper we explore the formation conditions of stellar winds on the basis of the TU-Berlin's modeling approach (Fleischer et al. 1992) with the goals of ascertaining the relations between mass loss rate and colors, of exploring their domain of validity, and, eventually, of uncovering their astrophysical significance.

According to the element composition of their surface layers, AGB stars divide themselves into oxygen-rich and carbon-rich sources depending on the value of the oxygen-to-carbon abundance ratio w.r.t. 1. In oxygen-rich sources the dust is made from oxides and metals ('silicates') whereas in carbon-rich sources the excess carbon is available for the formation of carbonaceous grains. In the following, we will mainly concentrate on C-rich sources and perform only a limited exploration of the case of O-rich sources.

In previous papers it has been demonstrated, that our approach is successful in producing models for the outflows from pulsating carbon-rich AGB stars which fit well their main characteristics: The models produce long-term variations and internal structures of the synthetic light curves, which are in agreement with respective near infrared light curves (Winters et al. 1994, 1997a). The spatial intensity profiles and spatial spectra show internal structures as well, which are also found in interferometric data and from lunar occultation observations (Winters et al. 1995, 1997b). This modeling approach has been applied to the extreme carbon star AFGL 3068 by Winters et al. (1997a), yielding the mass-loss rate and the outflow velocity, as well as the spectral energy distribution and its temporal variation and the light curves of the object. Moreover, the synthetic infrared CO line profiles in the (v 0-1) fundamental band (4.6 μm) and the (v 0-2) first overtone (2.3 μm) resulting from these models yield good agreement with the shape and the (long-term) temporal variation of the corresponding profiles observed from IRC +10216 (Winters 1998, Winters et al. 2000). Additionally, it has been demonstrated recently that the models produce molecular density enhancements in the shocked atmosphere, which very much resemble the main characteristics of the so-called *warm molecular layers* (Woitke et al. 1999, Helling & Winters 2000). A summary of the general infrared appearance of these models is given in Winters et al. (1999).

2. Presentation of the TU-model

2.1. General characteristics

The TU-model of red giant outflows is based on a time-dependent hydrodynamical description of a molecular atmosphere excited at its base by a periodic pulsation (Fleischer et al. 1992). The general effect of the pulsation is to enhance the density in the external layers of the stellar atmosphere where the temperature drops below 2000 K. The pulsation of the star initiates shock waves which are propagating outwards, thereby producing local density enhancements which provide favorable conditions for efficient dust formation. The avalanche-like outbreak of grain condensation in a layer results in an acceleration of this layer by radiation pressure on dust which in turn deeply modifies the atmospheric structure (Fleischer et al. 1991). Due to a dust-induced instability (*exterior κ–mechanism*, see Fleischer et al. 1995), the formation of a dust layer occurs on a time-scale which is generally longer than the pulsation period of the star, the dust shell possesses an eigenperiod.

The parameters of the TU-model are $M_\star$, the central star's present mass, L_0 and T_0, the central star's luminosity and temperature, P, the period of the pulsation, Δv_p, the velocity amplitude (at a level defined in Sect. 2.2) and the element abundances (see also Sect. 2.2). The parameters L_0 and T_0 refer to the hydrostatic initial model obtained for $\Delta v_p = 0$. The stellar radius, R_0, of the initial model then follows from Stefan-Boltzmann's law. We assume spherical symmetry of the star and of its circumstellar shell.

The code that is used here, has been submitted to a variety of tests. Also, the results have been compared satisfactorily to those of another, independent code using the same input physics, but a different numerical scheme (Höfner et al. 1996). We are therefore confident that the TU-model allows to explore correctly the behavior of outflows under a prescribed set of input physics which is detailed, together with a brief description of the modeling method, in the following section.

To investigate the effects of the different parameters we have built a grid of models which is based on a given choice of the input physics. The goal of the effort is to understand these effects rather than to attempt reproducing exactly some individual observed properties. Therefore the parameter combinations used for our grid might not always be realized in nature.

2.2. Hydrodynamic structure calculation

The set of equations describing time-dependent hydrodynamics, (equilibrium) chemistry, carbon dust formation, -growth and -evaporation and the (stationary, grey) radiative transfer problem are written in Lagrangian coordinates and discretized by means of the explicit, first-order scheme given in Richtmyer & Morton (1967).

Shocks are treated by means of an artificial tensor-viscosity according to Tscharnuter & Winkler (1979). To describe the relaxation of the gas after the passage of a shock, we adopt an LTE cooling law for the gas, i.e. $Q^{\mathrm{rad}} \sim \frac{\kappa^{\mathrm{g}}}{\rho}(T_{\mathrm{eq}}^4 - T_{\mathrm{g}}^4)$. Here, T_{g} is the gas temperature and T_{eq} is the radiative equilibrium

temperature, which equals the (grey) dust temperature $T_{\rm d}$ in our calculations.

We assume chemical equilibrium in the gas phase for a carbon-rich mixture and consider the concentrations of the species relevant for carbon grain formation (H, H_2, C, C_2, C_2H, and C_2H_2). We assume complete blocking of oxygen in the CO molecule and therefore no oxygen-bearing species are considered here.

Formation, growth and evaporation of carbon grains are treated by the moment method developed by Gail & Sedlmayr (1988) and Gauger et al. (1990), which takes into account thermal evaporation and chemical sputtering of the dust grains, as well as thermal non-equilibrium between the gas and the dust phase (i.e. $T_{\rm g} \neq T_{\rm d}$).

To calculate the radiative equilibrium temperature, $T_{\rm eq}$, the radiative transfer problem in the hydro-calculation is solved by a grey two-stream approximation for the spherical case according to the method of Unno & Kondo (1976) including the modifications described in Hashimoto (1995). For details see also Winters et al. (1997a).

The transport coefficients of the gas are replaced by a constant value for the opacity ($\kappa^{\rm g}/\rho = 2{\cdot}10^{-4}$ cm^2 g^{-1}, see Bowen 1988). To describe the dust extinction at this stage (hydrodynamic calculations), we replace the frequency-dependent dust opacity by its Planck-mean value, which in most cases is interpolated from a corresponding table derived from the Preibisch et al. (1993) data for amorphous carbon (aC), assuming the small particle limit of Mie theory.

The pulsation of the star is simulated by a sinusoidal variation of the velocity at the innermost grid point of the model (piston approximation)

$$v_{\rm i}(t) = \Delta v_p \cos(\frac{2\pi}{P}t) \ . \tag{1}$$

According to Eq. (1) the location of the inner boundary moves as

$$r_{\rm i}(t) = 0.91R_0 + \Delta v_p \frac{P}{2\pi} \sin(\frac{2\pi}{P}t) \ , \tag{2}$$

where the zero position of the piston at $0.91R_0$ is located at ≈ 2 pressure scale heights below the photosphere of the hydrostatic initial model. The value of $0.91R_0$ has been selected because it corresponds to the typical level just outside the hydrogen ionization zone which is supposed to drive the oscillation of the atmosphere (κ–mechanism).

To fix the inner boundary condition for the temperature structure, we assume a constant radiative flux entering the atmosphere at $r_{\rm i}$:

$$F(r_{\rm i}) = \frac{L_\star(t)}{4\pi r_{\rm i}^2(t)} = \frac{L_\star(0)}{4\pi r_{\rm i}^2(0)} = {\rm const}(t) \ . \tag{3}$$

From this boundary condition together with Eq. (2) it follows that the luminosity varies in time as

$$L_\star(t) = L_\star(0) \left(1 + a \sin(\frac{2\pi}{P}t) \left(2 + a \sin(\frac{2\pi}{P}t)\right)\right) \tag{4}$$

where

$$a = \frac{\Delta v_p}{r_{\rm i}(0)} \frac{P}{2\pi} = 0.041 \frac{\Delta v_p[\,{\rm km\,s^{-1}}]}{r_{\rm i}(0)\,[10^{13}{\rm cm}]} \, P\,[300\,{\rm d}] \ . \tag{5}$$

Since $a \ll 1$, the quadratic term in Eq. (4) is small and the luminosity varies almost sinusoidally. After solving for the temperature structure, the temporal development of the stellar temperature $T_\star$ and the stellar radius $R_\star$ can be calculated from the Stefan-Boltzmann law by means of the (implicit) consistency requirement

$$T(R_\star) = T_\star \tag{6}$$

(for details see Winters et al. 1997a).

For given values of $T_\star(t=0)$ and $L_\star(t=0)$ the initial stellar radius $R_\star(t=0)$ and the location of the inner boundary $r_{\rm i}(t=0) = 0.91R_\star(t=0) = 0.91R_0$ are fixed. Then, the velocity amplitude Δv_p and the pulsation period P directly influence the luminosity amplitude via Eqs. (4) and (5). The outer boundary for the hydro-calculation is put at 60 R_0.

The calculation is started with an hydrostatic, dust free model. The piston motion is slowly turned on and the evolution of the atmospheric structure is followed until a regular pattern has developed, which is usually well established after about 70 pulsation periods. All results presented here have been determined only after this transition 'switch-on' time interval.

The solution of the equation system is completely determined by the four stellar parameters: *stellar mass* $M_\star$, *stellar luminosity* $L_\star(t=0) = L_0$, of the hydrostatic initial model, *stellar temperature* $T_\star(t=0) = T_0$, of the hydrostatic initial model and the element abundances ϵ_i for which we basically assume a solar composition. To account for a carbon-rich mixture, the ratio $\epsilon_{\rm C}/\epsilon_{\rm O}$ is prescribed as a parameter of the model. Two additional parameters, the pulsation period P and the velocity amplitude Δv_p have to be specified to describe the velocity variation at the inner boundary simulating the pulsation of the star. For the pulsation period P we prescribe values in the range observed for AGB stars but we generally do not force the period to be consistent with the luminosity in terms of any period-luminosity relation. The stellar mass $M_\star$ is the actual mass, i.e. the present day mass of the star which is lower than the ZAMS mass due to mass loss on the main sequence, the red giant branch and the previous AGB phase.

The models are computed over at least 90 pulsation periods. We exclude variations on the evolutionary time scale of the star (e.g., $M_\star$ is taken to be constant). A typical time step in the hydro-calculation is of the order of 10^3 sec which results in about $5\,10^4$ time steps per pulsation period ($P \sim 500$ days). To resolve the radial structure we use 1024 mesh points. These hydro calculations are performed on a vector machine and one model-run over 90 periods typically takes of the order of 10 CPU-hours on a Cray T90.

2.3. Detailed radiative transfer calculation

After having determined the shell structure (previous section) we perform a frequency- and angle-dependent radiative transfer calculation, yielding the spectral energy distribution, the

monochromatic light curves, and the spatial appearance (intensity profiles) of the circumstellar dust shell (CDS) model. This detailed radiative transfer calculation is performed by means of a Feautrier scheme according to the method of Mihalas & Hummer (1974) (see Winters (1994) for details).

The transport coefficients of the gas are again represented by a constant value for the opacity ($\kappa^{\rm g}/\rho = 2 \cdot 10^{-4}$ cm^2 g^{-1}). To describe the frequency-dependent dust opacity, in most of the cases presented here we use the complex refractive index for amorphous carbon grains given by Preibisch et al. (1993), and apply the small particle limit of Mie theory. The frequency dependent radiative transfer calculation is performed every $0.05P$ for a time lapse usually of about $20P$ after the matter had been lifted to at least $60R_0$ (i.e. the outer boundary of the hydrodynamical calculations). At this distance dust formation and growth are basically completed and the velocity has reached an almost constant value which we identify with the terminal velocity. For doing the radiative transfer calculation, the density is extrapolated from $60R_0$ to an outer boundary (located at $2000\,R_0$ in the calculations presented here) by assuming a constant outflow velocity equal to this terminal velocity (hence a density $\propto {\rm r}^{-2}$ in the region outside $60R_0$). This extrapolation is performed in order to cover also the cool outer regions of the shell which by thermal emission contribute to the emergent infrared radiation of the CDS.

At the innermost grid point ($r_{\rm i}(t)$, see Sect. 2.2) the diffusion approximation is applied as the inner boundary condition for solving the radiative transfer equation, while for the outer boundary condition (at $2000\,R_0$), we assume that there is no inward directed radiation field.

The detailed radiative transfer is performed on a parallel computer. Each calculation takes about 3 CPU-sec on a Cray T3E, using 32 processor elements with 63 frequency points, 1054 radial mesh points and 1062 impact parameters. Given the time resolution for the radiative transfer calculation of $\Delta t = 0.05P$, this gives a computing time of about 20 CPU-min for each model covering $20P$.

2.4. Definition of the resultant quantities

We have explored the dependence of the mass loss process on physical quantities by varying the parameters of the model. In many instances, we have selected sets of values which we considered useful for our understanding. The parameter space was therefore not covered uniformly. Also, in some cases we have selected sets which might not match real situations. The range of parameters covered by our present models is given in Table 1.

With this approach we aim at discovering the parameters, or the combination of parameters, which are important to describe the mass loss phenomenon and in particular to address the relationship between colors and mass loss.

The mass loss rate, $\dot{\rm M}$, is estimated as a time average over usually $20\,P$ of both, the local mass flux through a sphere at $45\,R_0$ and of the radially averaged mass flux through all shells between 30 and $60\,R_0$. In previous works, we have used the first definition. However, in some cases where the wind shows an irregular structure, the second definition gives a more reliable quantification of the mass loss rate. We have observed that depending on the radial structure of the wind the estimate of $\dot{\rm M}$ may change considerably up to a factor 3. Therefore, we have adopted an average mass loss rate, $\langle\dot{\rm M}\rangle$ (indicated by the superscript $^{\rm r}$ in Table 2), that we define as the time average (usually over $20\,P$) of the radial average of the mass flux from 30 to $60\,R_0$. To quantify the stability of the wind we compute the standard deviation $\sigma_{\rm rel}$ (w.r.t. time) of the radial average from 30 to $60\,R_0$ and of the local mass flux (Table 2). The terminal velocity, $\langle v_\infty\rangle$, and the dust–to–gas ratio, $\langle\rho^{\rm d}/\rho^{\rm g}\rangle$, given in the $^{\rm r}$-entry of Table 2 also are the time averages of the radial average between 30 and $60\,R_0$ of the velocity and the dust–to–gas ratio, repectively. In all figures and in all tables presented in this paper, (except Table 2, where both definitions are contained) we give the results of the second, radial and temporal, averaging procedure. The radial averaging procedure for calculating the mass loss rate very much resembles the usual methods used to derive mass loss rates from observations, since they generally involve some integral of the shell structure along the line of sight (e.g., in terms of column densities, optical depths, or integrated emissivities).

Table 1. Range of parameters covered by the model grid

$M_\star$ $[M_\odot]$	L_0 $[L_\odot]$	T_0 [K]	C/O	P [d]	Δu_p [km s^{-1}]
0.8–1.8	3000–24000	2200–3300	1.20–1.80	104–1000	0.5–8.0

Finally, the colors are estimated from the emergent spectra computed on top of the hydrodynamic model as time averages usually over $20\,P$. The color K–L', of specific concern for our studies, is also given in Table 2.

We consider mainly the dust formation in carbon-rich environments. For that case, we have mostly used the opacities as given by Preibisch et al. (1993) for amorphous carbon. To examine the effect of the opacity on the results, a few models have been computed using different tables for the optical constants for amorphous carbon. The respective models are listed in Table 10.

Differences have certainly to be expected in the case of an oxygen-rich chemistry. However, we expect also common trends arising from the presence of dust (whatever its composition) in the outflows. This issue is addressed in Sect. 4.2.

3. Results

3.1. Mass loss - color correlation

Fig. 1 displays the average mass loss rate versus the synthetic K-L' near-infrared color index for all models of the grid calculated with the dust opacities for amorphous carbon (aC) given in Preibisch et al. (1993). The empirical $\dot{M}$/K-L' correlation for C-stars (Le Bertre 1997, solid line) is also shown. This relation was established for the range $1 \leq$K-L'≤ 8 and is extrapolated in the figure beyond these limits. In fact a non-variable M5 giant

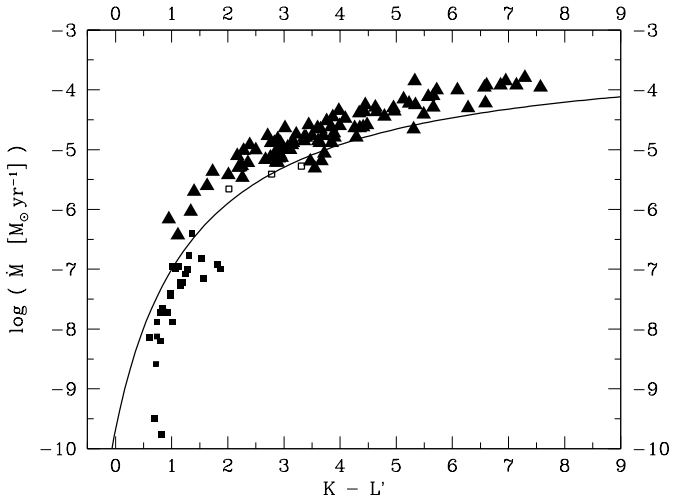

Fig. 1. Mass loss rate $\dot{M}$ vs. K-L' for all models of the grid calculated with the Preibisch et al. (1993) dust opacity. Filled triangles: A-models, filled squares: B-models, empty squares: AB models (see Sect. 3.2). Solid line: empirical correlation for C-stars (Le Bertre 1997)

(without circumstellar shell) would have a K-L' $\sim$ 0.2 (Bessell & Brett 1988).

The models with mass loss rates $\dot{M} \gtrsim 3 \cdot 10^{-7} M_{\odot}\mathrm{yr}^{-1}$ (filled triangles) follow a trend parallel to the observed correlation. These models will be hereafter referred to as A-models (see Sect. 3.2 for a more rigorous definition). There is a general shift of the calculated mass loss rates with respect to the empirical correlation by about a factor of 2 towards higher mass loss rates. Also, the calculations show a rather large spread around the correlation. However, it should be recalled here that the models which have been computed do not in general correspond to existing sources. For instance, we have not forced the models to obey any period-luminosity relation. Some models might be over-luminous for carbon-rich AGB stars (cf. Table 1).

The models with a mass loss rate $\dot{M} \lesssim 3\,10^{-7} M_{\odot}\mathrm{yr}^{-1}$ show a different behavior. Those will be referred to as B-models (see again Sect. 3.2). They occupy the region $0.5 \leq$ K-L' ≤ 2 and $10^{-10} \lesssim \dot{M} \lesssim 10^{-7} M_{\odot}\mathrm{yr}^{-1}$, and generally fall below the empirical relation.

Three models with K-L' $\approx$ 2–3.5 and mass loss rates of a few $10^{-6} M_{\odot}\mathrm{yr}^{-1}$ (models w50, w57, w96, see Table 3) are indicated by open squares. These models show an oscillating behavior of the mass loss rate on a time scale of $\sim 10^2$ yr and will be referred to as AB models.

Additionally, we find four models (w45, w55, w83, and w85), which are labeled by "static state" in Tables 2, 4, and 5 and which are not shown in Fig. 1. During the initial phase of the calculation, where the piston motion is switched on and the atmospheric structure is changing from a hydrostatic one to a hydrodynamical one, material is expelled from the star. Normally, this material is moving outwards and is completely ejected. However, in these cases it appears to fall back and to induce an increase of the density in the region between 10 and 30 R_0. The mass loss rate of these models is decreasing steadily with time and the velocity is approaching zero, i.e. the circumstellar shell is approaching a static state after a transition phase, where material is falling back to the star. In the final static situation, an extended dusty layer surrounds the star at a distance of 10–30 R_0, which is supported by radiation pressure. As these models might be artifacts we have not considered them in the following discussion.

Finally, there are 8 models which are labeled by "no wind" in Table 2 (see also Tables 4 and 5). These models do not develop a wind structure at all, the calculation breaks down already during the initial phase, where the piston motion is switched on. This indicates, that there is no dynamical solution of the equation system for the respective combination of model parameters.

The fact, that a correlation exists between the mass loss rate and a near-infrared color index for A-models should be related to the mass loss mechanism. For any wind driving mechanism, the mass loss rate is determined in the sub-sonic wind region. Therefore, any diagnostic tool useful to obtain information about the mass loss mechanism must be sensitive to the conditions in the inner, sub-sonic region of the circumstellar shell. It should be expected that near-infrared color indices, e.g. K-L', are determined by the amount of dust present in this inner shell region and therefore meet this requirement (Le Bertre & Winters 1998, Le Bertre et al. 1998).

3.2. Dependence of the models on the radiative acceleration

In the case of a *dust driven wind*, the mass loss rate is determined by radiation pressure on dust. In the case of our pulsating models, the dust formation and growth process is supported by an increased density due to the dissipation of shock wave momentum. Therefore, on one hand the density in the dust-forming region is connected to the pulsation of the star, and on the other hand the outflow is generated by radiation pressure on dust. From the *static* equation of motion (i.e. the condition of hydrostatic equilibrium) it follows that a radiation driven wind is possible, if the outward directed radiative acceleration a^{rad} exceeds the gravitational pull a^{grav} in the region $r > r_0$:

$$\alpha \equiv \frac{a^{\mathrm{rad}}}{a^{\mathrm{grav}}} = \frac{\frac{4\pi}{c}\chi_H H}{\rho G \frac{M_r}{r^2}} = \frac{4\pi\chi_H r^2 H}{c\rho G M_r} > 1, \;\; (r > r_0) \; . \qquad (7)$$

(c: speed of light, χ_H: flux-mean extinction coefficient, H: Eddington-flux, ρ: mass density, G: gravitation constant, M_r: mass contained in a sphere of radius r)

In the models presented here, r_0 corresponds to the dust formation zone. If we assume conservation of the radiative energy ($r^2 H = L_{\star}/16\pi^2$), α becomes

$$\alpha = \frac{1}{4\pi c G} \frac{L_{\star}}{M_r} \frac{\chi_H}{\rho} \; . \qquad (8)$$

In our pulsating models, α is a time-dependent quantity, which exhibits a layered radial distribution due to the factor χ_H/ρ (see e.g. upper panel in Fig. 5). The condition $\alpha > 1$ can be re-written in terms of an Eddington-like luminosity:

$$\alpha > 1 <=> L_{\star} > L_{\mathrm{Edd}} = 4\pi c G \frac{M_r}{\frac{\chi_H}{\rho}} \; . \qquad (9)$$

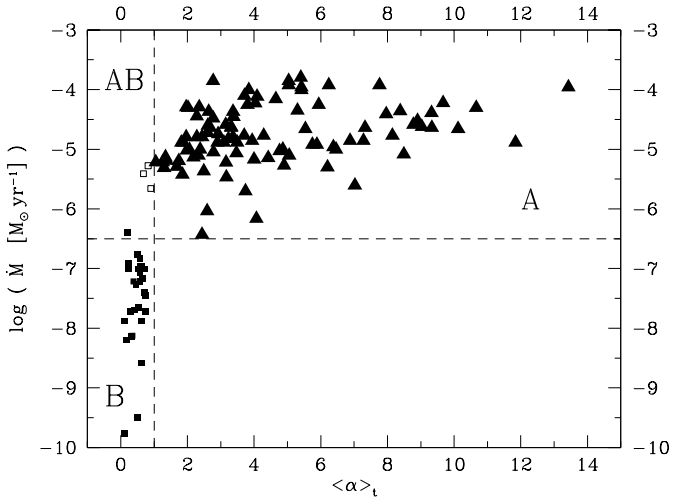

Fig. 2. Mass loss rate $\dot{M}$ vs. radiative acceleration $\langle\alpha\rangle_t$ for all models of the grid calculated with the Preibisch et al. (1993) opacity for amorphous carbon (aC). For the definition of regions A, B, and AB see Sect. 3.2

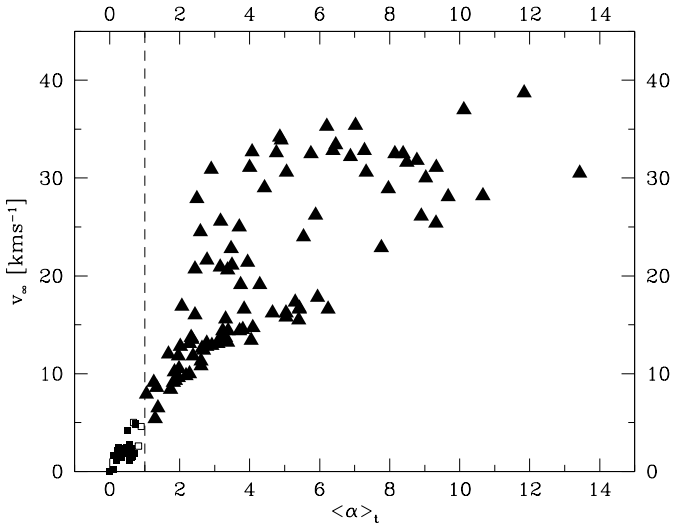

Fig. 3. Terminal wind velocity v_∞ vs. radiative acceleration $\langle\alpha\rangle_t$ for all models of the grid calculated with the Preibisch et al. (1993) opacity for amorphous carbon

However, χ_H/ρ itself depends in an intricate way on $L_\star$, $M_\star$, and $T_\star$, which makes the discussion of the wind driving mechanism in terms of a critical luminosity rather cumbersome. Therefore, in order to analyze the details of the wind driving mechanism in the pulsating models, we calculate a time averaged $\langle\alpha\rangle_t$ at the maximum of α in the innermost dust layer by defining:

$$\langle\alpha\rangle_t = \frac{1}{\Delta T}\int_{t_0}^{t_0+\Delta T} \max_r(\ \alpha(t)_{\rm innermost\ layer}\ )\,dt\,, \qquad (10)$$

where $\Delta T = n\cdot P$ is usually $20P$. $\alpha(t)$ is computed taking into account the gas and the dust opacity. However, in the calculations presented here, we have mostly used a rather small value of $\chi^{\rm g}_H/\rho = 2\cdot10^{-4}\,{\rm g\,cm^{-2}}$ for the gas opacity, so that in fact α is dominated by the dust opacity. For a more realistic treatment of the gas opacity see Sect. 4.1.

In Figs. 2 and 3, the mass loss rate $\dot{M}$ and the terminal wind velocity v_∞ are plotted versus the temporal average $\langle\alpha\rangle_t$ (Eq. (10)) for the models in the grid. The value $\langle\alpha\rangle_t = 1$ clearly defines two regions in Fig. 2. On the right of the corresponding vertical line we have models dominated by radiative acceleration (region A). On the left, the radiative acceleration is on average lower than the gravitational pull. A pronounced drop of the mass loss rate is evident from Fig. 2, when $\langle\alpha\rangle_t$ becomes less than unity. The horizontal line at $\dot{M} = 3\cdot10^{-7}M_\odot{\rm yr}^{-1}$ separates the mass loss rate of the models with $\langle\alpha\rangle_t > 1$ from the mass loss rates obtained for $\langle\alpha\rangle_t < 1$. However, there are three models with mass loss rates in excess of $10^{-6}M_\odot{\rm yr}^{-1}$ and $\langle\alpha\rangle_t < 1$ (open squares in Fig. 2, region AB). These models display an oscillating behavior of the mass loss rate and of $\langle\alpha\rangle_t$ (see below).

In general the winds of A-models have mass loss rates $\dot{M} > 10^{-6}M_\odot{\rm yr}^{-1}$ and all have terminal wind velocities $v_\infty > 5\,{\rm km\,s^{-1}}$ (Fig. 3). Models in zone A behave as dust driven winds, i.e. the pulsation of the star does not have a relevant influence on the wind properties. From analytical considerations of stationary, purely dust driven winds, Gail & Sedlmayr (1987) derive a minimum mass loss rate for C-stars of the order of $10^{-6}M_\odot{\rm yr}^{-1}$ (see also Lamers & Cassinelli 1999, Chap. 7). A similar value was obtained from a self consistent numerical solution of the stationary dust driven wind problem by Dominik et al. (1990). Here we find about the same value for the minimum mass loss rate (a few $10^{-7}M_\odot$ yr^{-1}) also in the case of pulsation supported dust driven outflows.

On the left side of the line defined by $\langle\alpha\rangle_t = 1$, the models concentrate in the lower part of the diagram where $\dot{M} < 3\cdot10^{-7}M_\odot{\rm yr}^{-1}$ (region B). For all these models, the expansion velocity, v_∞, is $< 5\,{\rm km\,s^{-1}}$ (see Fig. 3). In these cases, the radiative acceleration plays a minor rôle.

A few models with $\langle\alpha\rangle_t < 1$ have a mass loss rate $> 10^{-6}M_\odot{\rm yr}^{-1}$ (region AB, open squares). Their parameters are given in Table 3. For these models, we have performed follow-up calculations over a time lapse of up to about 500 P. These models display an oscillating variation of the mass loss rate on a typical time scale of $\sim 100\,P$ with variations of about a factor of 3–5 (see Fig. 4). The average mass loss rate of these models is of the order of a few $10^{-6}M_\odot{\rm yr}^{-1}$, accompanied by low outflow velocities around $5\,{\rm km\,s^{-1}}$. It should be noted here, that there is a time delay between the current value of α, which is determined in the inner region of the shell around $3\,R_0$ and the mass loss rate, which is evaluated in the region outside of $30\,R_0$. This time delay amounts to about 60 yr or 50 P for a typical stellar radius of a few 10^{13} cm, an outflow velocity typical for the AB models of $5\,{\rm km\,s^{-1}}$ and a typical period of 400 d. The temporal variation of the mass loss rate and of α in the innermost dust layer for model w50 is shown in Fig. 4 over a time lapse of $505\,P$, corresponding to 415 yr. The average values given for model w50 in the Tables 2 and 3 have been obtained over the last $40\,P$ only, and therefore differ slightly from the values given in Fig. 4. The AB-models and their possible relation to

Table 3. Models in zone AB

No.	$M_\star$ $[M_\odot]$	L_0 $[L_\odot]$	T_0 [K]	C/O	P [d]	Δv_p [km s^{-1}]	$\dot{M}$ [$M_\odot$yr^{-1}]	v_∞ [km s^{-1}]	$\rho^{\rm d}/\rho^{\rm g}$ 10^{-3}	K-L'	$\langle\alpha\rangle_t$
w50	0.8	4500	2600	1.30	300	5.0	3.9e-06	5.0	1.1	2.78	0.68
w57	1.0	5000	2600	1.30	400	5.0	5.3e-06	2.6	1.1	3.31	0.82
w96	1.0	6000	2800	1.30	400	5.0	2.2e-06	4.6	0.9	2.02	0.90

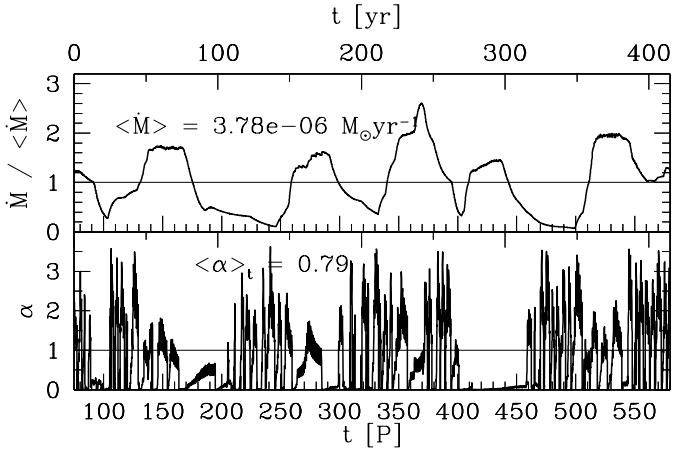

Fig. 4. Time variation of α and $\dot{M}$ of the AB-model w50. Upper panel: time variation of the radially averaged mass loss rate, lower panel: time variation of the radiative acceleration in the innermost dust layer

the observed multiple shells around the carbon-rich AGB star IRC +10216 (Mauron & Huggins 1999, 2000) and some proto-planetary nebulae, e.g., CRL 2688 (Sahai et al. 1998) will be investigated in detail in a forthcoming paper.

3.3. Typical radial structure of A- and B-models

In Fig. 5 the radial structure of model w29 ($M_\star = 0.80\,M_\odot$, $L_0 = 1.5\,10^4\,L_\odot$, $T_0 = 3000$ K, C/O= 1.50, $P = 800$ d, $\Delta v_p = 5$ km s^{-1}), representative of an A-model, is shown at a fixed instant of time. The model exhibits a clear layered structure of the dust distribution (e.g., α and f_c), accompanied by strong shocks propagating through the shell. These shocks are accelerated by radiation pressure on dust. The wind becomes supersonic in the region around $3R_0$ and the escape velocity is surmounted at around $7R_0$. Due to compression by the shocks, the density in the region just behind the shock fronts is strongly enhanced. The steps in the temperature structure are caused by efficient back-warming from the dust layers. Due to the rather effective LTE cooling assumed here, the gas temperature shows only small peaks in the shocked regions.

Fig. 6 displays the time variation of the two different estimates of the mass loss rate for model w29. The local mass flux (upper panel of Fig. 6) clearly reflects the layered structure of the shell. Each layer moving through the sphere at $45R_0$ produces a peak in the mass loss rate caused by the enhanced density in the wake of the accompanying shocks. The lower panel of Fig. 6 depicts the temporal variation of the mass flux averaged radi-

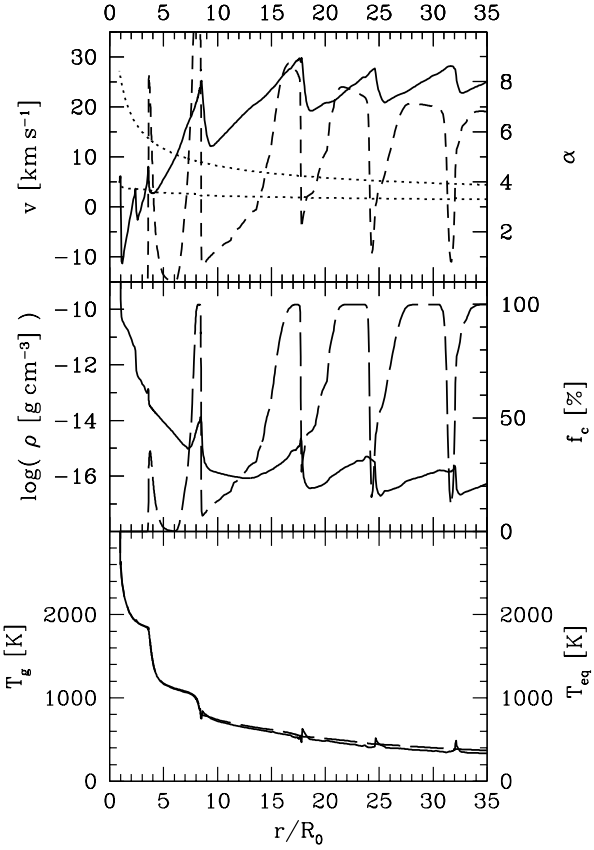

Fig. 5. Radial structure of a typical A-model (w29 at $t = 90\,P$). Upper panel: hydrodynamic velocity (solid line), escape velocity (upper dotted line), and isothermal sound speed (lower dotted curve) (l.h.s. ordinate) and radiative acceleration in units of the gravitational pull α (dashed line, r.h.s. ordinate). 2^{nd} panel: mass density ρ (solid line, l.h.s. ordinate) and degree of condensation f_c (dashed line, r.h.s. ordinate). Lower panel: gas temperature $T_{\rm g}$(solid line) and equilibrium temperature $T_{\rm eq}$ (dashed line)

ally in the region between 30 and $60R_0$ which largely smoothes the layered structure (note the different scaling of the ordinates in Fig. 6). We note that there is a slight difference between the values of both estimates of the mass loss rate for A-models. The normalized standard deviation is given for both averaging procedures in Table 2. For the temporal average at $45\,R_0$, $\sigma_{\rm rel}$ is around 1, which means that the mass loss rate is changing rapidly with time due to the layered structure of the wind. For the second averaging method adopted here, the standard deviation typically is in the range 0.1 to 0.3, which means that the

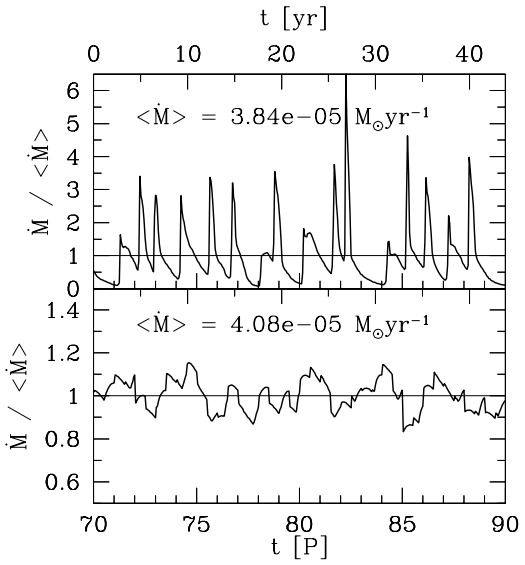

Fig. 6. Time variation of the mass loss rate of a typical A-model (w29). Upper panel: local mass flux through a sphere at $r = 45\,R_0$, lower panel: time variation of the radially averaged mass loss rate. Note the different scaling of the ordinates

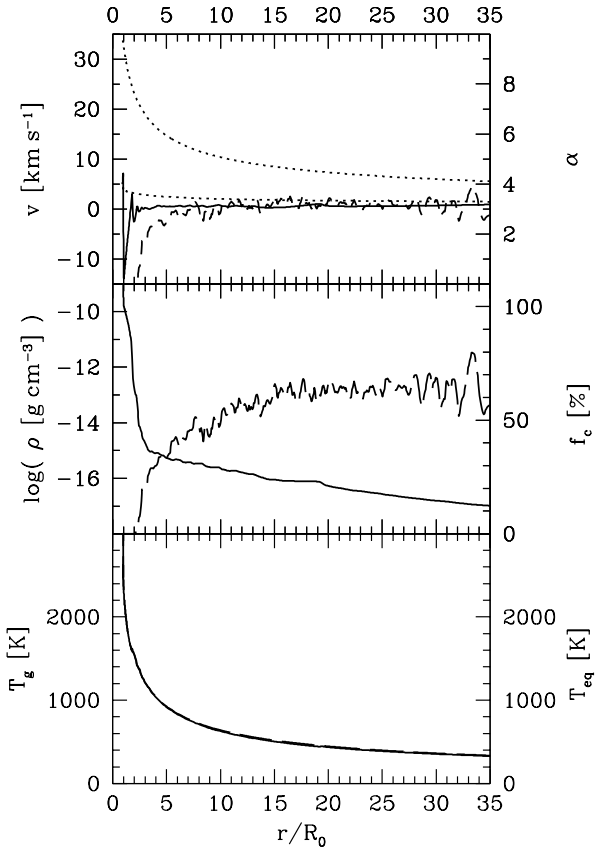

Fig. 7. Same as Fig. 5 for a typical B-model (w79 at $t = 490P$)

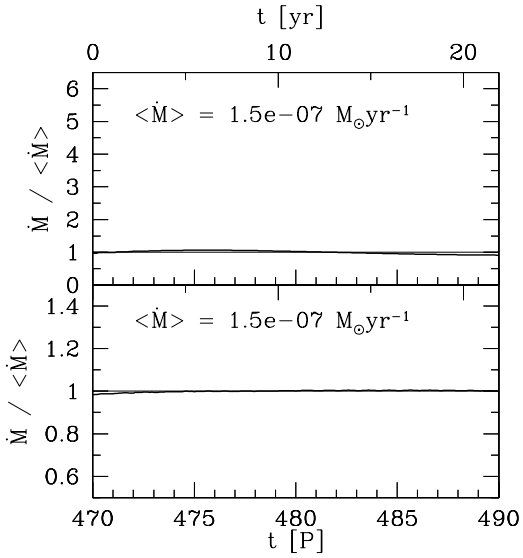

Fig. 8. Same as Fig. 6 for a typical B-model (w79)

layered structure as a whole is maintained almost identical over time.

In contrast, the radial structure of a typical B-model (w79, $M_\star = 1.20\,M_\odot$, $L_0 = 1\,10^4 L_\odot$, $T_0 = 2\,800$K, C/O$= 1.30$, $P = 400$ d, $\Delta v_p = 5$ km s^{-1}), shown in Fig. 7, is characterized by a much smoother distribution of the hydrodynamic and of the dust quantities, it does not present a layered structure. The degree of condensation remains comparably small ($\sim 65\%$) and, accordingly, the radiative acceleration is much less efficient. In particular, high α values are only reached at larger radial distances from the star than in the case of an A-model. Nevertheless, since the radiative force drops like r^{-2}, the acceleration is almost negligible here. As a result, the hydrodynamic velocity stays small, the sound speed is only reached at about 30 R_0 while the escape velocity is surmounted only at about 70 R_0. As a result, the mass loss rate is relatively low ($\dot{M} \sim 10^{-7} M_\odot$yr^{-1}) and almost constant in time (see Fig. 8).

3.4. Typical light curves of A- and B-models

In Fig. 9 the light curves of the same A-model (w29, l.h.s.) and B-model (w79, r.h.s.) are shown. Model w29 ($\dot{M} = 4.1\,10^{-5} M_\odot$yr^{-1}, $\rho^{\rm d}/\rho^{\rm g} = 2.4\,10^{-3}$) produces a multi-periodic light curve, reflecting the dynamics of the dust formation process which is governed by a time scale of its own (see Winters et al. 1994, Fleischer et al. 1995). Opposite trends of the mean magnitude at short and long wavelengths can be seen, e.g. around $t = 75P$ and $t = 80P$. This inversion is produced by the absorption of short wavelength radiation by the dust and re-emission of the energy at longer wavelengths. In this model, the luminosity amplitude is about 0.84 mag, while e.g., the average V amplitude amounts to ≈ 7 mag, the amplitude in K is 1.8 mag and the [12] amplitude is 0.63 mag. These results fit well the observations obtained on carbon Miras for which the light curve amplitudes decrease with wavelength with the same kind of values (e.g., Le Bertre 1992). On the other hand, the B-model w79 ($\dot{M} = 1.5\,10^{-7} M_\odot$yr^{-1}, $\rho^{\rm d}/\rho^{\rm g} = 1\,10^{-3}$) displays rather regular, small amplitude light curves. Here, the luminosity amplitude is about 0.45 mag and the V amplitude is

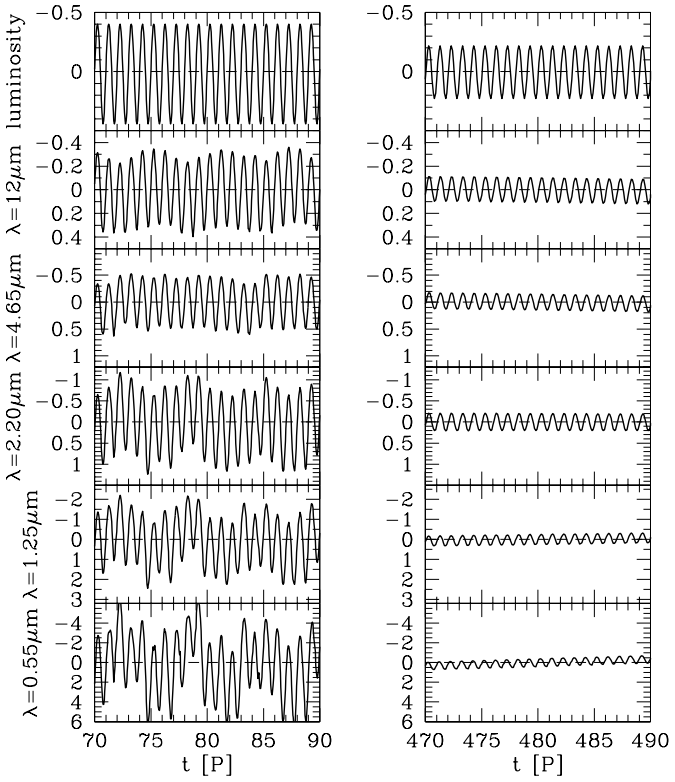

Fig. 9. Light curves (in magnitudes, relative to the mean magnitude) of a typical A-model (w29, l.h.s.) and a typical B-model (w79, r.h.s) for different wavelengths. The upper panels display the luminosity variation (see Eqs. (4) and (5)). Note the different scaling of the ordinates at different wavelengths (the same scaling is kept for both models to facilitate the comparison)

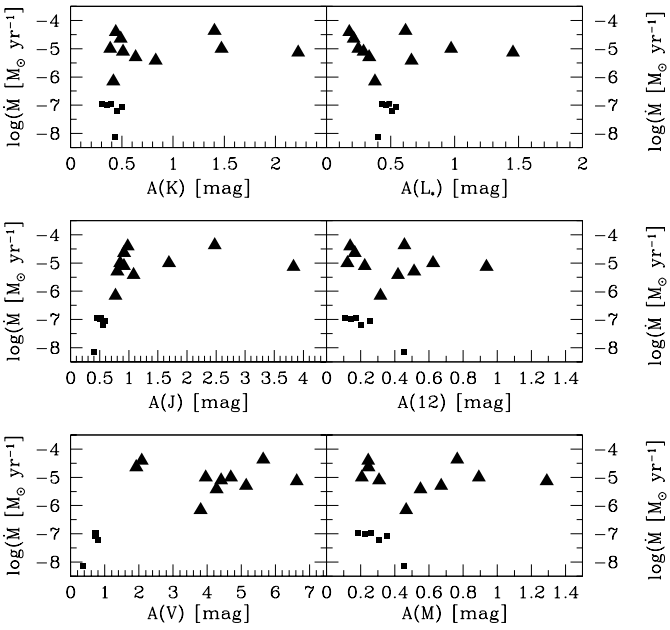

Fig. 10. Mass loss rates as a function of the light curve amplitudes and of the luminosity amplitude (in magnitudes) for 16 models of the grid

only 0.76 mag (A(K) = 0.41 mag, A(12) = 0.21 mag). These values are more typical of those obtained on Semiregular variables (SRa). Presently we have not attempted to reproduce the erratic light curves of the other Semiregular variables (SRb and SRc). In the A-models, the light curve amplitudes as well as their temporal variation are largely influenced by the processing of the radiation field by dust whereas the light curves of the B-models are mainly determined by the prescribed temporal variation at the inner boundary (piston).

Fig. 10 displays the mass loss rate as a function of the light curve amplitudes at different wavelengths and as a function of the luminosity amplitude (upper r.h.s. panel in Fig. 10) for a sub-set of models chosen to cover the whole range of mass loss rates. The different scaling of the abscissa for the amplitudes at different wavelengths reflects the observed decrease of the light curve amplitudes for increasing wavelength. From Fig. 10 one can see, that there is no correlation between the light curve amplitudes and the mass loss rate, neither for short nor for long wavelengths. The dispersion of the mass loss rates in the region of small luminosity amplitudes (upper r.h.s. panel in Fig. 10) illustrates that the mass loss rates are not governed by the assumed pulsation characteristics of the model. However, if a model is in region A (filled triangles), the amplitude of the visual light curve is always larger than 2 mag. This feature is typical of A models, where dust is forming in single layers close to the star. Due to the large opacity at short wavelengths, even a small variation of the amount of dust in this inner region of the shell causes a large variation in, e.g., the V magnitude.

3.5. Effects of the parameters

To investigate the effects of each individual parameter, we have compiled models which differ by only this specific parameter. These compilations are given in Tables 4–10 and allow to isolate the effects of L_0 (Table 4), $M_\star$ (Table 5), T_0 (Table 6), C/O (Table 7), P (Table 8), Δv_p (Table 9) and of the carbon dust opacity (Table 10). One finds a general trend: larger mass loss rates and larger color indices are favored by larger values of L_0, C/O, P and Δv_p, and by smaller values of $M_\star$ and T_0. For small values of the former and large values of the latter the models tend to be of the B class and for the reverse, they tend to be of the A class. In general, the transition from B to A occurs sharply, indicating that there exists a limiting value for each parameter which has to be surmounted in order to arrive at a dust driven wind solution.

3.5.1. Dependence on the luminosity

Increasing the stellar luminosity, all other parameters being kept identical, results in increasing the mass loss rate (Table 4). Arndt et al. (1997) have found a dependence of $\dot{M} \propto L_0^{1.5}$. This relation applies to the models well inside of region A but the dependence becomes much steeper in the transition zone to region B. From Table 4 it can be seen, that the critical luminosity below which the model moves to zone B depends on the combination of the other parameters. A high stellar temperature, e.g.,

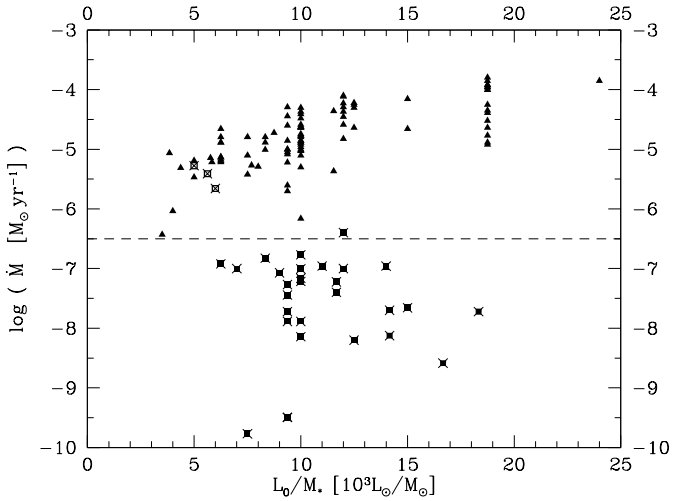

Fig. 11. Mass loss rate vs. $L_0/M_\star$ for all models of the grid calculated with the Preibisch et al. (1993) opacity. Triangles: A-models, open squares: AB models, filled squares: B-models. Crosses indicate an outflow velocity $v_\infty < 5\,\mathrm{km\,s^{-1}}$

requires a much higher stellar luminosity to produce a stable wind in zone A. In particular, with $M_\star = 1\,M_\odot$, C/O$= 1.30$, $P = 400\,$d, $\Delta v_p = 5\,\mathrm{km\,s^{-1}}$, and a temperature of $3000\,$K we do not obtain an A-model for reasonable values of the luminosity.

3.5.2. Dependence on the stellar mass

Increasing the stellar mass results in reducing the mass loss rate (Table 5). Besides the simple effect of the increased gravitation potential, this can be expected as the atmospheric scale height is proportional to $1/M_\star$ and therefore the amount of condensible matter in the critical region decreases with increasing $M_\star$. It is noteworthy that $\langle\alpha\rangle_t$ depends strongly on $M_\star$ at the transition from zone A to zone B (compare w57 with w44). Again, the Arndt et al. (1997) formula ($\dot{M} \propto M_\star^{-2.9}$) applies only to the A-models.

3.5.3. Combined effect of luminosity and mass

In Fig. 11 we show the combined effect of luminosity and stellar mass on the mass loss rate. Also in this diagram a separation between A-models and B-models can be seen, it is indicated by the limiting line at a mass loss rate of $3 \cdot 10^{-7} M_\odot \mathrm{yr}^{-1}$. All models below this limiting line have outflow velocities below $5\,\mathrm{km\,s^{-1}}$, indicated by the crosses in Fig. 11 (B-models). We recall that also the AB models (open squares) have a low outflow velocity although their mass loss rate is in excess of $10^{-6} M_\odot \mathrm{yr}^{-1}$. As would be expected from a consideration in terms of a simple Eddington luminosity, there is a limiting value of $L_0/M_\star \approx 3500\,L_\odot/M_\odot$, below which we should not find wind solutions of type A. On the other hand, we find B-models which have $L_0/M_\star-$ ratios $> 5000 L_\odot/M_\odot$. This is due to the dependence of χ_H/ρ on the other stellar parameters (temperature, C/O ratio, period, and piston amplitude), i.e. even for high $L_0/M_\star-$ ratios α can be less than 1 for an unfavorable combination of the other parameters.

3.5.4. Dependence on the stellar temperature

An increase of the stellar temperature results in a strongly decreasing mass loss rate (Table 6). This can be understood as when the stellar temperature is increased the nucleation region (at a typical temperature of $\approx 1300\,$K in the C-rich models) moves outwards, hence toward lower densities. The transition from zone A to zone B occurs abruptly, the mass loss rate drops by 2 orders of magnitude in an extremely narrow temperature interval (compare w130 with w131, and w137 with w148). We note that the outflow velocity might be slightly increasing with T_0 when a large amount of dust is formed (e.g., models in the lower part of Table 6), whereas the degree of condensation f_c (hence, the dust-to-gas ratio) is getting smaller. This paradox can be explained by the wavelength dependence of the dust extinction which makes short wavelength photons more efficient for the momentum transfer and, thus, for the acceleration of the wind in the supersonic region.

3.5.5. Dependence on the carbon abundance

Increasing the C/O ratio leaves the mass loss rate almost unaffected if the model is in zone A (Table 7). There is however a lower limit of the C/O ratio (depending on the combination of all other parameters), below which the model falls in region B. The effect can be spectacular (w79 versus w126). The reason is, that increasing the carbon abundance is equivalent to increasing the density of condensible material. However, once the model is in region A, a further increase of the carbon abundance increases the dust-to-gas ratio and, hence, considerably increases the outflow velocity of the wind but leaves the mass loss rate almost unaffected (compare w108 with w109). This is in agreement with the findings of Dominik et al. (1990) and Habing et al. (1994) for stationary dust driven wind models. Note, that all models in the grid with outflow velocities in excess of $v_\infty = 30\,\mathrm{km\,s^{-1}}$ have a rather high C/O-ratio of 1.80.

3.5.6. Dependence on the period

An increase of the pulsation period leaves the mass loss rate and also the terminal velocity almost unaffected if the model is well inside region A (Table 8). There is however a lower limit of the pulsation period (for a given set of all other parameters), below which the model lies in region B (w128 versus w113). It is noteworthy that this behavior has already been found from observations (see Fig. 1 in Jura 1986). When the period is increased, the matter is lifted further away from the central star, which favors dust condensation and reduces the effective gravitation. However, once a regime of efficient dust formation has been reached, the hydrodynamics becomes dominated by radiation pressure on dust and the effect of the pulsation period becomes marginal. For the range of parameters that we have considered, this situation is reached for $P \geq 300\,$days. There-

Table 4. Effect of varying the stellar luminosity

No.	$M_\star$ $[M_\odot]$	L_0 $[L_\odot]$	T_0 [K]	C/O	P [d]	Δv_p [km s^{-1}]	$\dot{M}$ $[M_\odot \mathrm{yr}^{-1}]$	v_∞ [km s^{-1}]	$\rho^{\mathrm{d}}/\rho^{\mathrm{g}}$ 10^{-3}	K-L'	$\langle\alpha\rangle_t$	type
w133	1.0	3000	2600	1.80	650	2.0	—	—	—	—	—	no wind
w134	1.0	3500	2600	1.80	650	2.0	3.7e-07	20.7	3.2	1.11	2.44	A
w132	1.0	4000	2600	1.80	650	2.0	9.2e-07	24.5	3.2	1.34	2.59	A
w10	1.0	5000	2600	1.80	650	2.0	3.4e-06	25.6	3.3	2.26	3.17	A
w09	1.0	7500	2600	1.80	650	2.0	7.9e-06	30.6	4.0	2.89	5.05	A
w01	1.0	10000	2600	1.80	650	2.0	1.0e-05	33.4	4.1	3.08	6.46	A
w08	1.0	15000	2600	1.80	650	2.0	2.2e-05	37.0	4.1	3.65	10.12	A
w45	0.8	3000	2600	1.30	400	5.0	-8.5e-09	-0.25	0.9	4.85	0.39	"static state"
w135	0.8	3500	2600	1.30	400	5.0	4.9e-06	5.4	1.2	3.55	1.30	A
w46	0.8	4000	2600	1.30	400	5.0	6.5e-06	6.5	1.2	3.67	1.38	A
w44	0.8	5000	2600	1.30	400	5.0	1.3e-05	9.1	1.2	3.64	1.82	A
w51	0.8	6000	2600	1.30	400	5.0	1.6e-05	10.0	1.2	3.90	2.28	A
w103	1.0	8000	3000	1.30	400	5.0	—	—	—	—	—	no wind
w105	1.0	9000	3000	1.30	400	5.0	8.5e-08	1.7	0.6	1.25	0.58	B
w76	1.0	10000	3000	1.30	400	5.0	6.1e-08	2.0	0.5	1.19	0.38	B
w106	1.0	11000	3000	1.30	400	5.0	1.1e-07	2.0	0.5	1.12	0.60	B
w102	1.0	12000	3000	1.30	400	5.0	1.0e-07	2.3	0.5	1.07	0.52	B
w104	1.0	14000	3000	1.30	400	5.0	1.1e-07	2.3	0.4	1.01	0.62	B

Table 5. Effect of varying the stellar mass

No.	$M_\star$ $[M_\odot]$	L_0 $[L_\odot]$	T_0 [K]	C/O	P [d]	Δv_p [km s^{-1}]	$\dot{M}$ $[M_\odot \mathrm{yr}^{-1}]$	v_∞ [km s^{-1}]	$\rho^{\mathrm{d}}/\rho^{\mathrm{g}}$ 10^{-3}	K-L'	$\langle\alpha\rangle_t$	type
w44	0.8	5000	2600	1.30	400	5.0	1.3e-05	9.1	1.2	3.64	1.82	A
w57	1.0	5000	2600	1.30	400	5.0	5.3e-06	2.6	1.1	3.31	0.82	AB
w85	1.2	5000	2600	1.30	400	5.0	-1.6e-08	-0.8	1.2	3.47	0.89	"static state"
w02	0.8	10000	2600	1.80	650	2.0	2.3e-05	31.1	4.3	4.26	9.33	A
w01	1.0	10000	2600	1.80	650	2.0	1.0e-05	33.4	4.1	3.08	6.46	A
w03	1.3	10000	2600	1.80	650	2.0	5.4e-06	33.9	3.1	2.25	4.90	A
w04	1.6	10000	2600	1.80	650	2.0	6.8e-06	31.1	3.1	2.67	4.00	A
w136	1.8	10000	2600	1.80	650	2.0	—	—	—	—	—	no wind

fore, any relation between the period and the mass loss rate for well developed winds ($\sim$ zone A) should come from an hidden relation (e.g. a relation between the period and the luminosity).

3.5.7. Dependence on the piston amplitude

The effect of increasing the piston amplitude is similar to the one of the period (Table 9): increasing the piston amplitude moves the material to larger distances from the star which favors dust formation and reduces the effective gravitation. There is a strong dependence of the mass loss rate and of the outflow velocity in the transition region, when the model changes from zone A to zone B (compare w89 and w12). Once the model is settled in zone A, an increase of the piston amplitude tends to slightly increase the mass loss rate, but the effect is not very pronounced.

Summarizing Sects. 3.5.1–3.5.7 we find that there exists a limiting value for each of the model parameters, below which (L_0, C/O, P, Δv_p), or above which ($M_\star$, T_0) the stable wind solution breaks down and the model moves to zone B, i.e. the model fails to produce an $\langle\alpha\rangle_t > 1$. The critical value of the respective parameter depends on the combination of the other parameter values. We note that $\langle\alpha\rangle_t = 1$ acts as a kind of 'switch' between the A and the B solutions, i.e. the state of the model changes almost discontinuously at $\langle\alpha\rangle_t = 1$.

3.6. Dependence on the dust opacity

The optical constants of the grains depend on the dust material and also on the microscopic structure of the particles. In the case of an ordered (crystalline) structure one finds a $1/\lambda^2$-dependence of the FIR extinction, while a disordered (amorphous) structure exhibits a $1/\lambda$-dependence (e.g., Wirsich 1987). In the case of carbon dust, both structures, *amorphous carbon* and crystalline *graphite* are possible.

The actual structure of the grains formed in carbon-rich stellar winds is not known a priori. Spectral modeling (e.g., Jura 1983, 1986; Sopka et al. 1985; Martin & Rogers 1987; Le Bertre 1987; Griffin 1990; Orofino et al. 1990; Bagnulo et al. 1995) favors a λ^{-n} law with $n \propto 1.2$–1.4, pointing towards the presence

Table 6. Effect of varying the stellar temperature

No.	$M_\star$ $[M_\odot]$	L_0 $[L_\odot]$	T_0 [K]	C/O	P [d]	Δv_p [km s^{-1}]	$\dot{M}$ $[M_\odot \mathrm{yr}^{-1}]$	v_∞ [km s^{-1}]	$\rho^{\mathrm{d}}/\rho^{\mathrm{g}}$ 10^{-3}	K-L'	$\langle\alpha\rangle_t$	type
w125	0.8	7500	2400	1.50	104	5.0	1.4e-05	21.4	2.2	3.61	3.94	A
w130	0.8	7500	2550	1.50	104	5.0	6.0e-06	20.9	2.3	2.36	3.16	A
w131	0.8	7500	2575	1.50	104	5.0	3.6e-08	4.8	0.5	0.97	0.75	B
w129	0.8	7500	2600	1.50	104	5.0	1.9e-08	4.9	0.5	0.93	0.75	B
w118	0.8	7500	3000	1.50	104	5.0	3.2e-10	4.2	0.0	0.69	0.50	B
w07	1.0	10000	2200	1.80	650	2.0	3.9e-05	28.9	4.2	5.49	7.96	A
w06	1.0	10000	2400	1.80	650	2.0	2.3e-05	30.6	4.2	4.35	7.33	A
w01	1.0	10000	2600	1.80	650	2.0	1.0e-05	33.4	4.1	3.08	6.46	A
w05	1.0	10000	3000	1.80	650	2.0	5.0e-06	35.3	2.4	2.19	6.20	A
w137	1.0	10000	3200	1.80	650	2.0	6.9e-07	32.7	2.3	0.95	4.07	A
w148	1.0	10000	3300	1.80	650	2.0	7.2e-09	1.5	0.8	0.61	0.31	B

Table 7. Effect of varying the carbon abundance

No.	$M_\star$ $[M_\odot]$	L_0 $[L_\odot]$	T_0 [K]	C/O	P [d]	Δv_p [km s^{-1}]	$\dot{M}$ $[M_\odot \mathrm{yr}^{-1}]$	v_∞ [km s^{-1}]	$\rho^{\mathrm{d}}/\rho^{\mathrm{g}}$ 10^{-3}	K-L'	$\langle\alpha\rangle_t$	type
w147	1.0	10000	2600	1.20	650	2.0	6.9e-08	1.5	0.6	1.56	0.64	B
w12	1.0	10000	2600	1.30	650	2.0	7.9e-06	13.7	1.0	2.17	2.33	A
w11	1.0	10000	2600	1.50	650	2.0	1.3e-05	21.1	2.0	2.94	3.49	A
w01	1.0	10000	2600	1.80	650	2.0	1.0e-05	33.4	4.1	3.08	6.46	A
w79	1.2	10000	2800	1.30	400	5.0	1.5e-07	1.1	1.0	1.53	0.57	B
w126	1.2	10000	2800	1.40	400	5.0	9.8e-06	16.9	1.5	2.50	2.06	A
w108	1.2	10000	2800	1.50	400	5.0	1.6e-05	20.6	2.0	3.39	3.37	A
w109	1.2	10000	2800	1.80	400	5.0	1.3e-05	30.9	3.6	3.16	2.90	A
w151	0.8	15000	3000	1.30	650	2.0	9.3e-06	16.3	1.1	1.87	2.09	A
w27	0.8	15000	3000	1.50	650	2.0	1.2e-05	26.2	1.8	2.39	5.88	A
w18	0.8	15000	3000	1.80	650	2.0	1.3e-05	38.7	3.9	2.83	11.84	A
w34	0.8	15000	2200	1.30	650	2.0	1.4e-04	15.8	1.4	6.95	5.04	A
w33	0.8	15000	2200	1.50	650	2.0	1.2e-04	22.9	2.6	7.14	7.76	A
w21	0.8	15000	2200	1.80	650	2.0	1.1e-04	30.5	4.3	7.57	13.43	A

Table 8. Effect of varying the pulsation period

No.	$M_\star$ $[M_\odot]$	L_0 $[L_\odot]$	T_0 [K]	C/O	P [d]	Δv_p [km s^{-1}]	$\dot{M}$ $[M_\odot \mathrm{yr}^{-1}]$	v_∞ [km s^{-1}]	$\rho^{\mathrm{d}}/\rho^{\mathrm{g}}$ 10^{-3}	K-L'	$\langle\alpha\rangle_t$	type
w127	0.8	5000	2600	1.30	250	5.0	1.2e-07	2.4	0.8	1.81	0.24	B
w49	0.8	5000	2600	1.30	300	5.0	7.4e-06	8.6	1.1	2.96	1.34	A
w110	0.8	5000	2600	1.30	350	5.0	6.4e-06	8.4	1.1	3.47	1.74	A
w44	0.8	5000	2600	1.30	400	5.0	1.3e-05	9.1	1.2	3.64	1.82	A
w111	0.8	5000	2600	1.30	500	5.0	1.3e-05	9.3	1.2	3.85	1.88	A
w112	0.8	5000	2600	1.30	600	5.0	1.6e-05	9.6	1.2	4.29	1.96	A
w128	0.8	7500	2600	1.30	200	5.0	5.4e-08	2.4	0.6	1.16	0.47	B
w113	0.8	7500	2600	1.30	300	5.0	1.0e-05	11.8	1.0	2.93	2.38	A
w48	0.8	7500	2600	1.30	450	5.0	2.5e-05	11.3	1.2	3.99	2.61	A
w114	0.8	7500	2600	1.30	600	5.0	5.1e-05	11.8	1.3	5.66	1.96	A
w141	0.8	7500	2600	1.30	800	5.0	3.6e-05	13.1	1.2	4.79	2.28	A
w138	1.0	10000	2600	1.80	200	2.0	9.4e-06	32.6	3.8	2.86	4.76	A
w17	1.0	10000	2600	1.80	300	2.0	1.4e-05	32.2	3.9	3.16	6.88	A
w16	1.0	10000	2600	1.80	450	2.0	1.1e-05	32.8	3.8	3.07	6.38	A
w01	1.0	10000	2600	1.80	650	2.0	1.0e-05	33.4	4.1	3.08	6.46	A
w15	1.0	10000	2600	1.80	800	2.0	1.4e-05	32.8	4.0	3.36	7.28	A

Table 9. Effect of varying the piston amplitude

No.	$M_\star$ $[M_\odot]$	L_0 $[L_\odot]$	T_0 [K]	C/O	P [d]	Δv_p [km s^{-1}]	$\dot{M}$ $[M_\odot \mathrm{yr}^{-1}]$	v_∞ [km s^{-1}]	$\rho^{\mathrm{d}}/\rho^{\mathrm{g}}$ 10^{-3}	K-L'	$\langle\alpha\rangle_t$	type
w152	1.0	10000	2600	1.80	650	0.5	8.0e-06	32.8	3.7	2.59	4.94	A
w86	1.0	10000	2600	1.80	650	1.0	1.2e-05	32.5	3.8	3.14	5.75	A
w01	1.0	10000	2600	1.80	650	2.0	1.0e-05	33.4	4.1	3.08	6.46	A
w87	1.0	10000	2600	1.80	650	3.0	1.7e-05	32.5	4.2	3.70	8.15	A
w88	1.0	10000	2600	1.80	650	4.0	2.4e-05	30.0	4.2	4.41	9.03	A
w13	1.0	10000	2600	1.80	650	5.0	2.6e-05	31.8	4.3	4.48	8.78	A
w14	1.0	10000	2600	1.80	650	8.0	5.0e-05	28.2	3.9	6.28	10.66	A
w89	1.0	10000	2600	1.30	650	1.0	1.7e-07	1.8	0.8	1.31	0.49	B
w150	1.0	10000	2600	1.30	650	1.5	7.4e-06	12.5	1.0	2.06	2.34	A
w12	1.0	10000	2600	1.30	650	2.0	7.9e-06	13.7	1.0	2.17	2.33	A
w90	1.0	10000	2600	1.30	650	3.0	2.3e-05	12.4	1.2	3.60	2.68	A
w91	1.0	10000	2600	1.30	650	4.0	3.3e-05	12.8	1.3	4.09	2.77	A
w36	0.8	15000	2200	1.30	300	2.0	9.9e-05	16.7	1.4	6.09	5.42	A
w38	0.8	15000	2200	1.30	300	5.0	1.1e-04	16.6	1.4	6.57	5.42	A
w37	0.8	15000	2200	1.30	300	8.0	1.2e-04	16.6	1.4	6.86	6.24	A

of "amorphous" rather than crystalline grains in the circumstellar shells around C-stars. This result is consistent with physical considerations, predicting the formation of inhomogeneous grains with crystalline cores surrounded by amorphous mantles (Gail & Sedlmayr 1984). Unfortunately, even for "amorphous" grains, the optical properties depend sensitively on their exact internal structure (e.g. the degree of crystallization and the hydrogen content, cf. Blanco et al. (1995), Koike et al. (1995)), which in turn is sensitive to the physical conditions of their production. For instance, in the case of "amorphous" carbon grains there exist several sets of data for the complex refractive index in the literature which are obtained from laboratory measurements performed under different experimental conditions (cf. Bussoletti et al. 1987).

Several works, which make use of such optical constants (e.g., Martin & Rogers 1987, Griffin 1990, Orofino et al. 1990, Bagnulo et al. 1995) have been performed. However, these studies were mainly focused on the spectral modeling of circumstellar dust shells, neglecting the influence of different opacities on the dynamical structure of the shell and on the resulting global hydrodynamical quantities characterizing the outflow (e.g., the mass loss rate and the final wind velocity). Recently, two independent investigations have been presented by Fleischer et al. (1999) and by Andersen et al. (1999) who explore the rôle of different carbon grain opacities on the wind properties in terms of time-dependent hydrodynamical models. Both groups find that the mass loss rate turns out to be rather independent of the extinction data used, whereas the terminal wind velocity as well as the dust-to-gas ratio and also the spectral energy distributions depend on the optical data used. In the present work, the data from Preibisch et al. (1993) have been preferred because they were derived for carbon grains produced in an hydrogen-bearing atmosphere (BE-sample) which seems to be more appropriate for an AGB star environment than the hydrogen deficient AC sample. Additionally, the Preibisch et al. optical constants are available for a broad wavelength region ($0.1\,\mu\mathrm{m} \leq \lambda \leq 800\,\mu\mathrm{m}$).

To investigate the influence of different dust opacity data on the models in terms of the $\dot{M}-$color index relations, we have calculated three different models (i.e. different sets of model parameters) using three different tables for the dust optical constants for each model. The optical data where taken from Maron (1990) (M), Preibisch et al. (1993) (P), and from Edoh (1983) (E), each of them appropriate for "amorphous carbon". According to the slope n of the extinction efficiency Q, represented in the small particle limit as

$$\frac{Q(a,\lambda)}{a} \equiv Q'(\lambda) = Q'_0 \left(\frac{\lambda_0}{\lambda}\right)^n , \qquad (11)$$

the tables can be ordered in a sequence of increasing n like M: $n \approx 1.19$ ($Q'_0 = 9149\,\mathrm{cm}^{-1}$); P: $n \approx 1.38$ ($Q'_0 = 14814\,\mathrm{cm}^{-1}$); E: $n \approx 1.46$ ($Q'_0 = 19202\,\mathrm{cm}^{-1}$) in the wavelength range $1.65\,\mu\mathrm{m} < \lambda < 3.8\,\mu\mathrm{m}$, where $\lambda_0 = 2.2\,\mu\mathrm{m}$. The characteristic wind properties resulting from these different opacity data are summarized in Table 10. The main result is that increasing the slope n and the magnitude Q'_0 leads to an increase of K-L' (as well as $\langle\alpha\rangle_t$ and v_∞) but leaves the mass loss rate $\dot{M}$ almost unaffected. As a result (Fig. 12), the slope of the empirical $\dot{M}$/K-L' relation is maintained with each of the optical data sets while the offset in $\dot{M}$ at given K-L' decreases with decreasing n (i.e. from Maron to Edoh via Preibisch et al.). Although outflow velocities up to about 40 km s^{-1} have been observed for a few AGB stars (e.g., Loup et al. 1993), the values listed in Table 10 are fairly high compared to the more typical values of 15–20 km s^{-1} observed for carbon stars. These high calculated velocities are mainly caused by the large C/O ratio used in the models listed in Table 10 (see Sect. 3.5.5 and also Sect. 4.1) and, therefore, cannot be used to rule out, e.g., the Edoh data for describing the optical properties of the grains actually formed in a C-rich stellar outflow.

Table 10. Effect of the dust opacity; M=Maron (1990), P=Preibisch et al. (1993), E=Edoh (1983)

No.	dust opac.	$M_\star$ $[M_\odot]$	L_0 $[L_\odot]$	T_0 [K]	C/O	P [d]	Δv_p [km s^{-1}]	$\dot{M}$ $[M_\odot \mathrm{yr}^{-1}]$	v_∞ [km s^{-1}]	$\rho^{\mathrm{d}}/\rho^{\mathrm{g}}$ 10^{-3}	K-L'	$\langle\alpha\rangle_t$	type
w66	M	1.0	10000	3000	1.80	650	2.0	4.6e-06	25.9	3.0	1.78	2.80	A
w05	P	1.0	10000	3000	1.80	650	2.0	5.0e-06	35.3	2.4	2.19	6.20	A
w115	E	1.0	10000	3000	1.80	650	2.0	5.2e-06	38.9	2.1	2.46	8.01	A
w67	M	1.0	10000	2600	1.80	650	5.0	2.8e-05	26.0	4.3	4.16	5.93	A
w13	P	1.0	10000	2600	1.80	650	5.0	2.6e-05	31.8	4.3	4.48	8.78	A
w116	E	1.0	10000	2600	1.80	650	5.0	2.3e-05	35.2	4.1	4.52	9.31	A
w68	M	0.8	10000	2200	1.80	650	2.0	6.6e-05	23.4	4.2	6.02	5.84	A
w20	P	0.8	10000	2200	1.80	650	2.0	6.0e-05	28.1	4.3	6.59	9.67	A
w117	E	0.8	10000	2200	1.80	650	2.0	6.0e-05	30.8	4.3	7.01	11.86	A

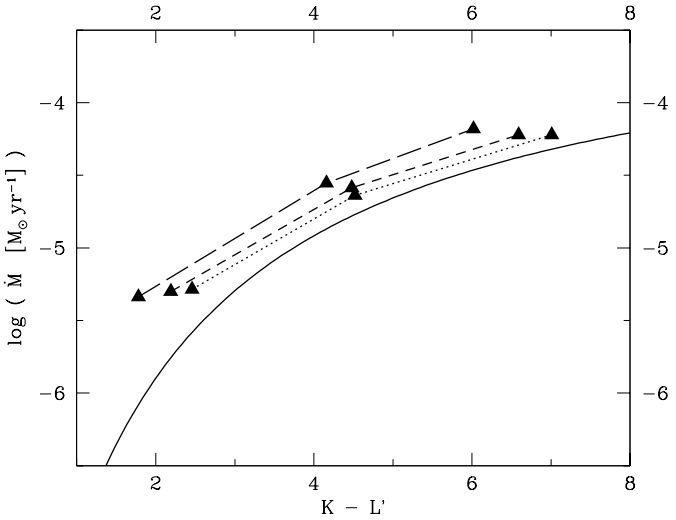

Fig. 12. Mass loss rate vs. K-L' for three models, each calculated with a different dust opacity (see Table 10). Long-dashed line: Maron (1990), short-dashed line: Preibisch et al. (1993), dotted line: Edoh (1983). Solid line: empirical correlation for C-stars

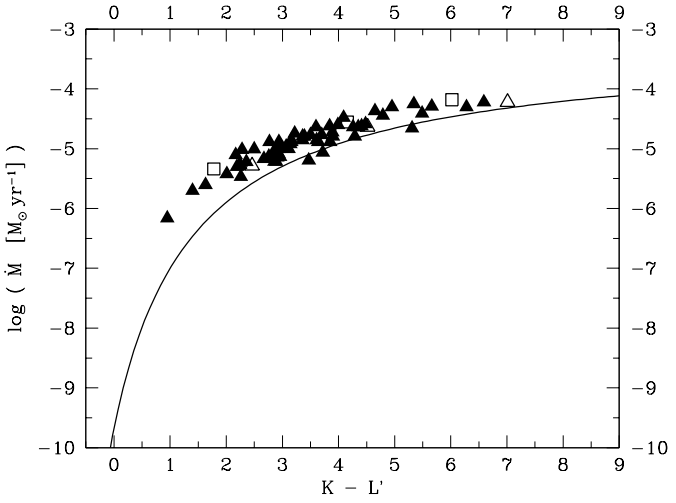

Fig. 13. Mass loss rate vs. K–L' for carbon-rich A-models with luminosities in the range $5\,10^3 L_\odot < L_0 < 10^4 L_\odot$ (see Sect. 3.7). Filled triangles: Preibisch aC, open squares: Maron aC, open triangles: Edoh aC

3.7. Implications for the observed color-mass loss relations

Real mass-losing carbon-rich Miras have periods in the range 300–700 days which corresponds to a luminosity range $4.5\,10^3 \leq L_\star \leq 11\,10^3$ (Groenewegen & Whitelock 1996). From the discussion in Sect. 3.5.1 it appears that by reducing the range of the luminosity in the model grid, we would reduce the width of the correlation for the models. Also, as the points corresponding to the large mass loss rates come from models with $L_0 \geq 15\ 10^3 L_\odot$, excluding these models would bring the average of the models closer to the observed relation.

In Fig. 13, we have selected carbon-rich models with $5\,10^3 L_\odot < L_0 < 10^4 L_\odot$ and $v_\infty > 5$ km s^{-1} (i.e. all B-models have been removed with this second criterion). With this selection we obtain a better agreement between the models and the observed correlation, although a small shift still remains.

With the same selection we also obtain a good agreement between models and observations in the J–K versus $\dot{M}$ diagram (Fig. 14).

For the K–12 versus $\dot{M}$ diagram (Fig. 15), the selected models follow the same trend as the observations but we have a larger shift again. Actually, it seems that the shift increases with wavelength. This λ-dependence points towards an effect of the dust opacity. In Sect. 3.6, we have seen that the choice of the optical data mainly affects the colors but not so much the mass loss rates of the models. Figs. 13–15 display also the three models calculated with the Maron (1990) optical constants (open squares) and those calculated with the Edoh (1983) data (open triangles). It seems that using the Edoh data would bring the models much closer to the empirical correlation by increasing the color index of the models with almost unchanged mass loss rate.

As a conclusion it seems that the total shift observed in Fig. 1 could result from the combination of two effects: presence of models with too large luminosities, which increase the mass loss rate at given near-infrared color index, and an inadequacy of the Preibisch et al. dust optical data, producing too small values of the color index at given mass loss rate.

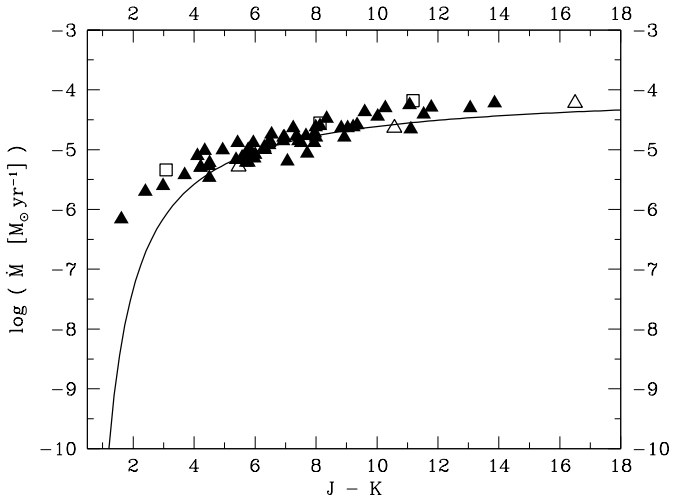

Fig. 14. Mass loss rate vs. J-K for carbon-rich A-models with luminosities in the range $5\,10^3 L_\odot < L_0 < 10^4 L_\odot$ (see Sect. 3.7). Filled triangles: Preibisch aC, open squares: Maron aC, open triangles: Edoh aC

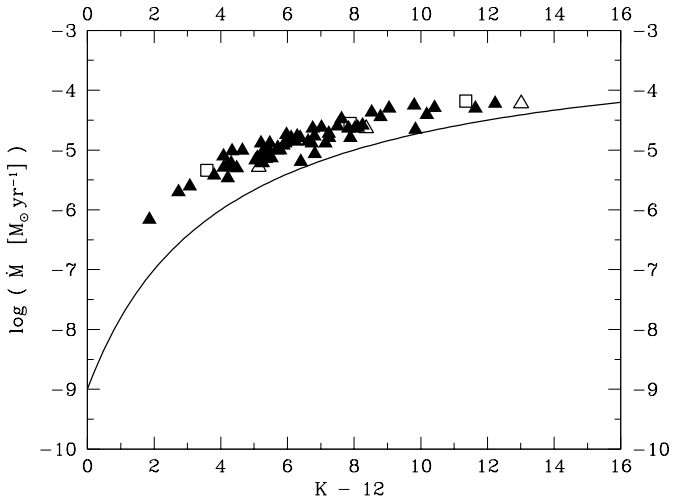

Fig. 15. Mass loss rate vs. K–12 for carbon-rich A-models with luminosities in the range $5\,10^3 L_\odot < L_0 < 10^4 L_\odot$ (see Sect. 3.7). Filled triangles: Preibisch aC, open squares: Maron aC, open triangles: Edoh aC

3.8. Winds with low expansion velocities

The terminal velocities of outflows from red giants can be measured from the profiles of CO rotational lines. On the basis of a large compilation of such data, Loup et al. (1993) have shown that most of the observed sources have terminal velocities, v_∞, in the range 5–30 km s^{-1}. A few sources have larger v_∞, up to 40 km s^{-1} (their Fig. 7). These results are in agreement with our findings for models in zone A. On the other hand there is a hint for the existence of a population of sources with v_∞ smaller than 5 km s^{-1}. Nyman et al. (1992) have shown that these sources are found preferentially in the region(s) II (and VII) of the IRAS [12–25, 25–60] two-color diagram (van der Veen & Habing 1988). Therefore, they might correspond to circumstellar shells with small optical depth. It is tempting to relate these sources to our models in zone B.

Recently, narrow CO line profiles have been observed for 2 sources, BM Gem (FWHM ~ 1 km s^{-1}, Kahane et al. 1998) and EU And (~ 5 km s^{-1}, Jura & Kahane 1999). The authors argue that the narrow CO emission lines are signatures of long-lived reservoirs of orbiting gas, and not of outflows. However, these stars are very peculiar; their evolutionary status is unclear and they may belong to binary systems. In BM Gem the narrow feature sits on a faint broader feature (~ 15 km s^{-1}) which would arise from a "normal" wind.

In another case, X Her, Kahane & Jura (1996) have also observed a narrow feature (~ 5 km s^{-1}) overimposed on a broad one (≥ 20 km s^{-1}). The CO emission here is interpreted as resulting from a slowly expanding spherical wind ($v_{exp} = 2.5$ km s^{-1}, $\dot{M} = 9\,10^{-8} M_\odot$yr^{-1}) and a bipolar flow ($v_{exp} \geq 10$ km s^{-1}). In a survey of 45 AGB stars observed in CO with good spectral resolution and good signal-to-noise ratio, Knapp et al. (1998) found evidence for 9 such composite profiles. They explain these profiles with the presence of 2 winds with different expansion velocities. In general, the slow wind has an expansion velocity smaller than 5 km s^{-1} and a mass loss rate smaller than $5\,10^{-7}$ M$_\odot$ yr^{-1}, and the opposite for the fast wind. In the context of our study, it is tempting to ascribe the slow wind to the B-type and the fast wind to the A-type models. We have shown in the previous sections that a slight change in the stellar parameters may induce a switch from one mode to the other. On the other hand, it is worth noting that in the case of X Her there is a shift in the spatial positions of the blue and red CO emission wings pointing to a real bipolar outflow.

In the Knapp et al. (1998) sample the slow winds are always associated with faster "normal" ones. There is a priori no reason for that, except possibly a selection bias in the sample favoring objects for which there is already an indication for a large mass loss rate ($\geq 10^{-7}$ M$_\odot$ yr^{-1}), and we would expect also sources with only a B-type wind. Young (1995) performed a volume limited (d $\leq$ 500 pc) survey of Miras. For most sources which have been detected, the CO lines can be fitted with a one–component wind. Several sources have expansion velocities ≤ 5 km s^{-1}, and one, T Ari, has a $v_{exp} = 2.7$ km s^{-1}, typical of our B models. Finally, Kerschbaum et al. (1996) measured $v_{exp} = 1.9$ km s^{-1} for the Semiregular variable L^2 Pup, a value again typical of a B-model.

Hence, there is growing evidence for the existence of sources with narrow (FWHM ≤ 8 km s^{-1}) CO line profiles. Jura & Kahane (1999) have proposed that this kind of emission could come from reservoirs of orbiting molecular gas. The B-type wind model that we have discovered in the present study offers an alternative explanation for these unusually narrow profiles. As the objects should be losing matter at a low rate and as the colors of the infrared sources should not be extreme (i.e. K-L ≤ 2, see Fig. 1), they may have escaped attention in the past. Also, the CO molecules might be more easily photodissociated in these tenuous circumstellar shells.

4. Prospects

From the discussion in Sect. 3.2, it is clear that $\langle\alpha\rangle_t$ is a key for understanding the properties of outflows from cool giants. The radiative acceleration results from the opacity which is the sum of two terms: the gas opacity and the dust opacity. In the following two sections, we briefly explore models for which the gas opacity is treated more realistically (Sect. 4.1) and models where the dust is of O-rich composition (Sect. 4.2).

4.1. Carbon-rich models with gas opacity tables

The rôle of molecular opacities for the dynamical structure of the CDS has recently been investigated by Helling et al. (2000). They use Rosseland and Planck mean gas opacities instead of the constant value $\kappa^{\rm g}/\rho = 2 \cdot 10^{-4}\,{\rm cm^2\,g^{-1}}$ (Bowen 1988) that we have used for our grid. Their models with Planck means give the largest opacity for the gas whereas ours have the smallest. To approximate the dust opacity, they generally use a Rosseland mean adopted from Gail & Sedlmayr (1985, GS). Still, three models have also been performed with the Preibisch et al. (1993) dust opacities (p01$R_{\rm g}$, p05$P_{\rm g}$, and p148$P_{\rm g}$, see Table 11). Helling et al. (2000) find, that a larger gas opacity causes a less dense atmosphere (a smaller scale height) so that there is less material available for grain condensation. Consequently, the mass loss rates are smaller as well as the expansion velocity and the dust-to-gas ratio (Table 11). Different dust opacities seem to affect the wind properties more strongly in the case of large gas opacities, i.e. at low overall densities (compare g05$P_{\rm g}$ and p05$P_{\rm g}$ versus g01$R_{\rm g}$ and p01$R_{\rm g}$). Due to the low gas density, the Planck-models (g05$P_{\rm g}$ and p05$P_{\rm g}$) are close to the A-B transition region, where the wind properties react sensitively to changes of the local conditions in the dust formation zone.

As the (small) constant value for the gas opacity provides a lower limit and the Planck mean an upper limit to the gas opacity, we expect that the real wind properties will correspond to an intermediate situation. Nevertheless, the Planck mean might give results closer to reality because of the effect of increased opacity arising from the Doppler shifts of the molecular lines due to the large velocity gradients in the shocked stellar atmosphere.

In the models discussed in Sect. 3, the radiative acceleration α is dominated by the dust opacity and the gas opacity plays a minor rôle. By contrast, in the Planck models α is much more dependent on the gas opacity, the effect being mostly important between the discrete layers of dust and in the inner region of the wind, below the first dust layer. Nevertheless, the mass loss rates stay smaller in the Planck models because the stellar atmospheres are less dense and the dust growth therefore is less efficient. As a result, the contribution of the dust opacity to α is reduced in the solar metallicity models, and the latter effect dominates over the increased gas opacity.

We note that the expansion velocities $v_\infty \approx 10$–$20\,{\rm km\,s^{-1}}$ obtained by a more realistic treatment of the gas opacity are closer to the observed velocities than those obtained in Sect. 3 (see Fig. 3). Therefore, a correct treatment of the gas opacity seems necessary to reproduce all the characteristics of carbon star outflows.

We have also started to compute models with LMC abundances. A decrease of the metallicity directly decreases the amount of condensible material but also decreases the gas opacity. As a result, due to the reduced amount of dust α is much smaller than in the solar metallicity models. The resulting very small mass loss rates and outflow velocities of the LMC models may raise the question of an additional momentum input to the atmosphere in order to efficiently drive the outflows of low-metallicity stars.

4.2. Oxygen-rich models

Finally, we consider a set of models with an oxygen-rich gas composition (Table 12) which has been obtained by Jeong (2000). These are the first, and so far unique, consistent O-rich outflow models. The treatment of the dust formation process is more complicated than in the carbon-rich case due to the more complex dust chemistry. For this reason, each model requires about a factor of 5 more CPU time than the models of the carbon-rich grid.

The dust formation appears to be heterogeneous with a core consisting of a high temperature condensate and a mantle composed of a variety of oxides. In the O-rich models, the core of the dust grains consists of TiO_2, which has been shown to be a good candidate for efficient nucleation in the temperature regime expected for the stars of our interest (Jeong et al. 1999). The dust growth involves all species which become stable at different positions in the wind, thereby providing a heterogeneous composition of the grain mantles. To describe the opacity of these "dirty" grains, we adopt the optical properties of "astronomical silicate" (Draine & Lee 1984) as tabulated in Draine (1985, DL, a = 0.1 μm) and for the gas opacity we use the same constant value of $\kappa^{\rm g}/\rho = 2 \cdot 10^{-4}\,{\rm cm^2\,g^{-1}}$ as in the carbon-rich grid.

Jeong (2000) has shown that efficient TiO_2 nucleation occurs at a typical temperature of $\sim 1000\,{\rm K}$ (about $300\,{\rm K}$ lower than in the carbon-rich case), corresponding to a radial zone between $3\,R_0 \ldots 5\,R_0$. Therefore, the densities in the dust formation region are also lower. Nevertheless, the same physical mechanism drives the outflow and the models display a similar hydrodynamic structure, although the dust layers are usually less pronounced than in the carbon-rich case. This is caused by the generally smaller amount of condensible material in the oxygen-rich situation and by the lower extinction efficiency of the oxygen-rich grains. Both facts reduce the dust extinction coefficient, and thus α, which makes it more difficult to drive the wind. Therefore, we had to use rather extreme values for the model parameters to obtain stable outflows (see Table 12). Since the winds here are also driven by radiation pressure on dust, we expect to have also correlations between color indices and mass loss rate. However, from the first six models calculated so far it is hard to estimate their behavior with respect to the relations observed for oxygen-rich Miras (see Fig. 16). Nevertheless, in Table 12 we note at least the same trends of the mass loss rate, outflow velocity and the color index with period and luminos-

Table 11. Effect of the gas opacity (R_g: Rosseland mean gas opacity, P_g: Planck mean gas opacity, * constant gas opacity: $\kappa^g/\rho = 2{\cdot}10^{-4}\mathrm{cm^2 g^{-1}}$) for solar abundances and for LMC abundances; GS=Gail & Sedlmayr (1985), P=Preibisch et al. (1993)

No.	dust opac.	$M_\star$ $[M_\odot]$	L_0 $[L_\odot]$	T_0 [K]	C/O	P [d]	Δv_p [km s^{-1}]	$\dot{M}$ $[M_\odot \mathrm{yr}^{-1}]$	v_∞ [km s^{-1}]	ρ^d/ρ^g 10^{-3}	K-L'	$\langle\alpha\rangle_t$
g01R_g	GS	1.0	10000	2600	1.80	650	2.0	2.3e-06	19.6	2.0	—	1.35
p01R_g	P	1.0	10000	2600	1.80	650	2.0	2.1e-06	21.1	1.9	1.46	1.44
w01*	P	1.0	10000	2600	1.80	650	2.0	1.0e-05	33.4	4.1	3.08	6.46
g05P_g	GS	1.0	10000	3000	1.80	650	2.0	5.9e-07	17.1	1.4	—	1.06
p05P_g	P	1.0	10000	3000	1.80	650	2.0	2.0e-07	11.5	0.6	0.86	1.08
w05*	P	1.0	10000	3000	1.80	650	2.0	5.0e-06	35.3	2.4	2.19	6.20
gxxP_g	GS	1.0	8000	3000	1.80	650	2.0	2.6e-07	21.4	1.7	—	1.37
g137P_g	GS	1.0	10000	3200	1.80	650	2.0	9.8e-08	11.1	0.5	—	0.36
w137*	P	1.0	10000	3200	1.80	650	2.0	6.9e-07	32.7	2.3	0.95	4.07
g148P_g	GS	1.0	10000	3300	1.80	650	2.0	4.6e-08	9.1	0.6	—	0.57
p148P_g	P	1.0	10000	3300	1.80	650	2.0	3.4e-08	8.9	0.4	0.69	0.50
w148*	P	1.0	10000	3300	1.80	650	2.0	7.2e-09	1.5	0.8	0.61	0.31
g01P_gLMC	GS	1.0	10000	2600	1.80	650	2.0	2.1e-10	0.1	0.7	—	0.56
g05P_gLMC	GS	1.0	10000	3000	1.80	650	2.0	6.2e-11	-0.3	0.2	—	0.95
g05R_gLMC	GS	1.0	10000	3000	1.80	650	2.0	9.9e-09	2.8	0.7	—	0.80

Table 12. Effect of oxygen-rich dust formation, dust opacity: "astronomical silicate" (Draine 1985)

No.	$M_\star$ $[M_\odot]$	L_0 $[L_\odot]$	T_0 [K]	C/O	P [d]	Δv_p [km s^{-1}]	$\dot{M}$ $[M_\odot \mathrm{yr}^{-1}]$	v_∞ [km s^{-1}]	ρ^d/ρ^g 10^{-3}	K-L'	$\langle\alpha\rangle_t$
v28	1.0	20000	2000	0.50	300	5.0	6.2e-05	16.3	4.2	2.41	1.28
v31a	1.0	15000	2000	0.50	300	5.0	2.7e-05	14.2	4.1	2.33	1.30
v33a	1.0	10000	2000	0.50	300	5.0	4.1e-06	11.4	4.0	1.55	0.98
v34a	1.0	8000	2000	0.50	300	5.0	4.4e-07	7.2	3.2	1.45	0.98
v34b	1.0	8000	2000	0.50	450	5.0	3.6e-06	8.2	4.1	1.78	0.45
v40	0.8	15000	2200	0.50	650	2.0	6.8e-05	16.7	4.0	2.54	2.23

ity as for the C-rich models. The present combination of input parameters is certainly not realistic for real M-type Miras, i.e. the temperatures are too low and the luminosities are too high.

5. Conclusions

We have found that the winds from pulsating, dust forming AGB star models separate into two classes depending on the value of $\langle\alpha\rangle_t$, a quantity which characterizes the importance of the radiative acceleration relative to the gravitational deceleration in the layer where dust is condensing. For $\langle\alpha\rangle_t$ larger than 1, radiation pressure on dust dominates the wind generation. The outflows are stable with characteristic layered structures (A-type winds). The mass loss rates are determined by the conditions in the sonic region and take values in the range $\sim 10^{-7} - 10^{-4} M_\odot \mathrm{yr}^{-1}$. For the models of the grid, the outflow velocities are in the range 5–40 km s^{-1} where the higher outflow velocities are found with high C/O ratios. On the other hand for $\langle\alpha\rangle_t$ smaller than 1, the radiation pressure is not sufficient to generate the winds. Here the pulsation of the central star becomes important for the mass loss phenomenon. These winds produce mass loss rates which are below $\sim 3 \cdot 10^{-7} M_\odot \mathrm{yr}^{-1}$ (B-type winds). The outflow velocity is relatively low, $v_\infty < 5\,\mathrm{km\,s^{-1}}$, since there is not enough dust to accelerate the wind. In a narrow transition region between zones A and B, we find a few models which develop winds showing long term variations (~ 100 yr time scale) of the mass loss rate by about a factor of 5 around a typical mean value of $\sim 10^{-6} M_\odot \mathrm{yr}^{-1}$. Also in these models, the outflow velocity is relatively low, $v_\infty \approx 5\,\mathrm{km\,s^{-1}}$.

In general, B-type winds are favored by small values of the stellar luminosity L_0, the C/O-ratio, the pulsation period P, and the pulsation amplitude Δv_p, and by large values of the stellar temperature T_0 and the stellar mass $M_\star$. The transition from a B to an A-type wind occurs sharply within a small range of these parameters.

For A-type winds, our model calculations show correlations between near-infrared color indices, noticeably K-L', and mass loss rates. However, we note a systematic shift with respect to the observed correlations which might be due to a combined effect of the luminosity and of the dust opacity law. A more realistic treatment of the gas opacity might also improve the situation.

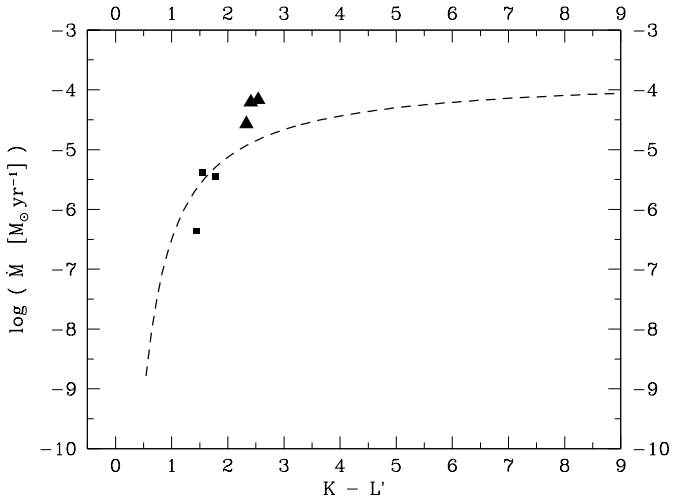

Fig. 16. Mass loss rate vs. K-L' for the oxygen-rich models listed in Table 12 computed with the DL dust opacity (Draine 1985). Filled triangles: $\alpha > 1$, filled squares: $\alpha < 1$, dashed line: empirical correlation for O-rich Miras (Le Bertre & Winters 1998)

The long-term oscillations of the mass loss rate resulting from the AB-type models might lead to a layered density structure in the extended circumstellar shell which resembles the characteristics of the multiple layers recently found in some carbon-rich proto-planetary nebulae and also in the shell of the prominent tip-AGB carbon star IRC +10216.

The behavior that we find for B-type models and the characteristics of the corresponding winds could provide an explanation for the presence of the mass losing low luminosity giants in the Galactic Bulge which have been reported by Omont et al. (1999) and Chan et al. (1998). We caution that this hypothesis should be handled with care as our present B-models are carbon-rich. Nevertheless, if the same mechanisms act for oxygen-rich outflows (and this seems to be the case, Sect. 4.2), then we would expect to find also O-rich B-type winds.

Acknowledgements. We are grateful to the referee for attracting our attention to the observations of low expansion velocity sources. The calculations were performed on the Cray parallel and vector computers of the Konrad-Zuse-Zentrum für Informationstechnik Berlin. Subsequent data analysis has been performed on the WAP–cluster of the physics department of the TU–Berlin. This work has been supported by the BMBF (grant 05 3BT13A 6), by the FAZIT Stiftung, by the DFG (grant Se 420/19–1), and by the PROCOPE program under grants D/9822849 (DAAD) and F/99001 (MAE).

References

Andersen A., Loidl R., Höfner S., 1999, A&A 349, 243
Arndt T.U., Fleischer A.J., Sedlmayr E., 1997, A&A 327, 614
Bagnulo S., Doyle J.G., Griffin I.P., 1995, A&A 301, 501
Bessell M.S., Brett J.M., 1988, PASP 100, 1134
Blanco A., Fonti S., Orofino V., 1995, ApJ 448, 339
Bowen G.H., 1988, ApJ 329, 299
Bussoletti E., Colangeli L., Borghesi A., Orofino V., 1987, A&AS 70, 257
Chan K.-W., Roellig T.L., Onaka T., Yamamura I., Tanabé T., 1998, ApJ 505, L31
Dominik C., Gail H.-P., Sedlmayr E., Winters J.M., 1990, A&A 240, 365
Draine B.T., 1985, ApJS 57, 587 (DL)
Draine B.T., Lee H.M., 1984, ApJ 285, 89
Edoh O., 1983, Ph.D. Thesis, University of Arizona (E)
Epchtein N., Le Bertre T., Lépine J.R.D., et al., 1987, A&AS 71, 39
Fleischer A.J., Gauger A., Sedlmayr E., 1991, A&A 242, L1
Fleischer A.J., Gauger A., Sedlmayr E., 1992, A&A 266, 321
Fleischer A.J., Gauger A., Sedlmayr E., 1995, A&A 297, 543
Fleischer A.J., Winters J.M., Sedlmayr E., 1999, In: Le Bertre T., Lèbre A., Waelkens C. (eds.) IAU Symp. 191, Asymptotic Giant Branch Stars. p. 187
Gail H.-P., Sedlmayr E., 1984, A&A 132, 163
Gail H.-P., Sedlmayr E., 1985, A&A 148, 183 (GS)
Gail H.-P., Sedlmayr E., 1987, A&A 177, 186
Gail H.-P., Sedlmayr E., 1988, A&A 206, 153
Gauger A., Gail H.-P., Sedlmayr E., 1990, A&A 235, 345
Griffin I.P., 1990, MNRAS 247, 591
Groenewegen M.A.T., Whitelock P.A., 1996, MNRAS 281, 1347
Habing H.J., Tignon J., Tielens A.G.G.M., 1994, A&A 286, 523
Hashimoto O., 1995, ApJ 442, 286
Helling Ch., Winters J.M., 2000, A&A submitted
Helling Ch., Winters J.M., Sedlmayr E., 2000, A&A 358, 651
Höfner S., Fleischer A.J., Gauger A., et al., 1996, A&A 314, 204
Jeong K.S., 2000, Ph.D. Thesis, Technische Universität, Berlin, FRG
Jeong K.S., Winters J.M., Sedlmayr E., 1999, In: Le Bertre T., Lèbre A., Waelkens C. (eds.) IAU Symp. 191, Asymptotic Giant Branch stars. p. 233
Jura M., 1983, ApJ 267, 647
Jura M., 1986, ApJ 303, 327
Jura M., Kahane C., 1999, ApJ 521, 302
Kahane C., Jura M., 1996, A&A 310, 952
Kahane C., Barnbaum C., Uchida K., Balm S.P., Jura M., 1998, ApJ 500, 466
Kerschbaum F., Olofsson H., Hron J., 1996, A&A 311, 273
Knapp G., Young K., Lee E., Jorissen A., 1998, ApJS 117, 209
Koike C., Kimura S., Kaito C., et al., 1995, ApJ 446, 902
Lamers H.J.G.L.M., Cassinelli J.P., 1999, Introduction to stellar winds. Cambridge University Press, Cambridge, UK
Le Bertre T., 1987, A&A 176, 107
Le Bertre T., 1992, A&AS 94, 377
Le Bertre T., 1997, A&A 324, 1059
Le Bertre T., Winters J.M., 1998, A&A 334, 173
Le Bertre T., Winters J.M., Sedlmayr E., 1998, In: Le Bertre T., Lèbre A., Waelkens C. (eds.) IAU Symp. 191, Asymptotic Giant Branch stars. Poster P3–06. ADS
Lépine J.R.D., Ortiz R., Epchtein N., 1995, A&A 299, 453
Loup C., Forveille T., Omont A., Paul J.F., 1993, A&AS 99, 291
Maron N., 1990, Ap&SS 172, 21 (M)
Martin P.G., Rogers C., 1987, ApJ 322, 374
Mauron N., Huggins P.J., 1999, A&A 349, 203
Mauron N., Huggins P.J., 2000, A&A 359, 707
Mihalas D., Hummer D.G., 1974, ApJS 28, 343
Nyman L.-Å., Booth R.S., Carlström U., et al., 1992, A&AS 93, 121
Olofsson H., 1999, In: Le Bertre T., Lèbre A., Waelkens C. (eds.) IAU Symp. 191, Asymptotic Giant Branch Stars. p. 3
Omont A., Ganesh S., Alard C., et al., 1999, A&A 348, 755
Orofino V., Colangeli L., Bussoletti E., Blanco A., Fonti S., 1990, A&A 231, 105

Preibisch T., Ossenkopf V., Yorke H.W., Henning T., 1993, A&A 279, 577 (P)
Richtmyer R.D., Morton K.W., 1967, Difference methods for initial-value problems. 2^{nd} edition John Wiley & Sons, New York
Rouleau F., Martin P.G., 1991, ApJ 377, 526
Sahai R., Trauger J.T., Watson K.R., et al., 1998, ApJ 493, 301
Sedlmayr E., 1994, In: Jørgensen U.G. (ed.) IAU Colloquium 146, Molecules in the Stellar Environment. Springer, p. 163
Sopka R.J., Hildebrand R., Jaffe D.T., et al., 1985, ApJ 294, 242
Tscharnuter W.M., Winkler K.-H., 1979, Comp. Phys. Comm. 18, 171
Unno W., Kondo M., 1976, PASJ 28, 347
van der Veen W.E.C.J., Habing H.J., 1988, A&A 194, 125
Winters J.M., 1994, Ph.D. Thesis, Technische Universität, Berlin, FRG
Winters J.M., 1998, Ap&SS 255, 257
Winters J.M., Fleischer A.J., Gauger A., Sedlmayr E., 1994, A&A 290, 623
Winters J.M., Fleischer A.J., Gauger A., Sedlmayr E., 1995, A&A 302, 483
Winters J.M., Fleischer A.J., Le Bertre T., Sedlmayr E., 1997a, A&A 326, 305
Winters J.M., Fleischer A.J., Sedlmayr E., 1997b, In: Paresce F. (ed.) Science with the VLT Interferometer. Springer, p. 403
Winters J.M., Le Bertre T., Keady J.J., 1999, In: Le Bertre T., Lèbre A., Waelkens C. (eds.) IAU Symp. 191, Asymptotic Giant Branch Stars. p. 261
Winters J.M., Keady J.J., Gauger A., Sada P.V., 2000, A&A 359, 651
Wirsich J., 1987, Infrared Phys. 27, 399
Woitke P., Helling Ch., Winters J.M., Jeong K.S., 1999, A&A 348, L17
Young K., 1995, ApJ 445, 872